Available online at www.sciencedirect.com

SCIENCE DIRECT®

Journal of Computational Physics 198 (2004) 535–566

JOURNAL OF
COMPUTATIONAL
PHYSICS

www.elsevier.com/locate/jcp

A finite volume formulation of compact central schemes on arbitrary structured grids

Chris Lacor [a,*], Sergey Smirnov [a], Martine Baelmans [b]

[a] *Department of Fluid Mechanics, Vrije Universiteit Brussel, Pleinlaan 2, Brussel 1050, Belgium*
[b] *Department of Mechanical Engineering, KULeuven, Celestijnenlaan 300A, Heverlee 3001, Belgium*

Received 16 June 2003; received in revised form 28 November 2003; accepted 15 January 2004
Available online 26 February 2004

Abstract

In the present paper a formulation allowing the use of compact schemes in the finite volume context on arbitrary meshes is presented. The proposed formulation is based on the use of an implicit formula to evaluate the fluxes on the cell faces. A series of numerical experiments for a 2D model convection equation, a flat plate, a subsonic vortical problem as well as the LES simulation of channel flow has been carried out. The results indicate an important improvement in obtained accuracy compared to a standard central finite volume formulation.

1. Introduction

In the solution of many physical problems, one is often confronted with flows possessing a wide range of space and time scales. In order to resolve all the scales of such flows, highly accurate methods, which can properly represent all the scales of the solution, are needed. In recent years, so-called compact (or Padé type) schemes [1,2] have gained increasing popularity in applications such as DNS [3], LES [4,5], and computational aeroacoustics [3,6,7], as an alternative to spectral methods. The main advantage of these schemes is that, while providing a better representation of the shorter length scales of solution, as compared to classical finite-difference and finite-volume schemes, they allow to use more complex mesh geometries, whereas spectral methods are limited to applications in simple domains and with simple boundary conditions. This better representation of the shorter length scales of the solution can be attributed to the implicit nature of these schemes. In the present paper the term 'compact' is used to refer to this implicit aspect. It does not necessarily imply that the proposed schemes are more compact than standard schemes with the same order of accuracy.

---

[*] Corresponding author.
E-mail address: chris.lacor@vub.ac.be (C. Lacor).

doi:10.1016/j.jcp.2004.01.025

Originally, compact schemes were defined in the finite-difference context, in one dimension and on a uniform grid. One of the first applications of compact finite-differencing to solving differential problems can be found in the book by Collatz [8,9].

However, it is only recently, in view of the applications mentioned above, that there is a renewed interest in these type of schemes.

An important issue is the use of compact schemes in multidimensions and their accuracy on general, i.e., non-Cartesian and also non-uniform grids.

In a finite-difference context, this is usually dealt with by formulating the compact schemes in the computational space, e.g. [10–14]. However, as mentioned in [3], the use of the Jacobian transformation can lead to an important reduction of the accuracy of the scheme in case of non-smoothly varying mesh spacings because of numerical errors in the determination of the derivatives of the transformation appearing in the Jacobians. Gamet et al. [3] take the non-uniformity of the mesh into account by adapting the coefficients of the compact stencils on Cartesian grids. If the grid is non-Cartesian, a Jacobian transformation still has to be used. Note that a similar approach was formulated earlier by Goedheer and Potters [15], for a second-order partial differential equation.

Although, in the framework of the finite-difference approach the compact schemes are relatively easy to construct on irregular grids, special attention must be paid to the conservation properties of the scheme, as the conservation is not automatically guaranteed.

The finite volume (FV) method, on the other hand, is inherently conservative. Until now, only few papers dealing with compact schemes in the FV context can be found in the literature.

To our knowledge, one of the first papers dealing with a formulation of compact schemes within the FV context is by Gaitonde and Shang [16]. The scheme is based on an implicit reconstruction step, relating cell face values to cell-averaged values. A similar approach is proposed more recently by Kobayashi [17]. However, both papers only deal with linear equations and uniform Cartesian grids. Straightforward extension on non-uniform Cartesian meshes or non-Cartesian meshes causes the scheme to loose its higher-order accuracy. It is to be noted that this is also the case for the standard central and MUSCL type schemes, which are often referred to as being second-order accurate whereas this is only the case on uniform Cartesian grids, the order on non-uniform and non Cartesian grids being (much) less.

In an attempt to formulate a higher-order accurate FV scheme on arbitrary grids, another route was followed in [18]. This approach is further detailed in the present paper and applied to a series of problems ranging from linear convection, Euler, laminar Navier–Stokes to a basic LES test problem.

It is to be mentioned that a similar approach was independently developed by Kobayashi and co-workers [19,20] as an extension of their work on linear equations to the non-linear incompressible Navier–Stokes system. Although results are only shown on Cartesian grids, the proposed formulation can also be used for non-Cartesian grids by working in computational rather than physical space. In that case, as already mentioned above, errors in the calculation of the derivatives of the transformation might reduce the global accuracy of the scheme, cf. [3]. This is why in the current paper a formulation in physical space is chosen.

The outline of the present paper is as follows. First, the approach in 1D is explained, both for linear convection and non-linear convection (Euler) and on uniform and non-uniform grids. Next, the method is extended to the multi-dimensional Euler and Navier–Stokes system. In a third section, results are shown for a series of test problems. The paper ends with the main conclusions.

2. Finite volume compact schemes in 1D

The main idea of a Padé type finite-difference scheme is to construct the approximation of the differential equation to be solved, with not only node values being unknowns, but also the derivatives. For the first derivative of any scalar quantity u, the Padé type approximation can be written as follows [1]:

$$\gamma u'_{i+2} + \kappa u'_{i+1} + u'_i + \kappa u'_{i-1} + \gamma u'_{i-2} = C\frac{u_{i+3} - u_{i-3}}{6h} + B\frac{u_{i+2} - u_{i-2}}{4h} + A\frac{u_{i+1} - u_{i-1}}{2h}, \tag{1}$$

where h is the grid-spacing (in the assumption of uniform mesh) and γ, κ, A, B, and C are coefficients that determine the accuracy of the approximation and which can be derived by developing all the variables in a Taylor series about point i, and requiring all the coefficients of the resulting expansion to vanish up to some definite term. The first non-zero coefficient will determine the formal truncation error.

Similarly, one can construct compact approximations for higher-order derivatives.

Let us now consider the following generic 1D advection equation

$$\frac{\partial u}{\partial t} + \frac{\partial f(u)}{\partial x} = 0. \tag{2}$$

This equation can represent a linear equation, in which case it is assumed that

$$f \equiv a \cdot u, \tag{3}$$

with 'a' a constant convection speed. Alternatively, Eq. (2) can be non-linear with $f(u)$ some non-linear relation.

In the FV approach, Eq. (2) is integrated over the mesh cells. For cell i, with cell faces $i - 1/2$ and $i + 1/2$, one obtains:

$$\frac{\partial}{\partial t}\int_{x_{i-1/2}}^{x_{i+1/2}} u\,\mathrm{d}x + f_{i+1/2} - f_{i-1/2} = 0. \tag{4}$$

This is still an exact relation, even if the mesh is non-uniform, i.e., the different cells have different widths. To discretize Eq. (4), both the integral and the fluxes on the interfaces $x = x_{i+1/2}$ and $x = x_{i-1/2}$ must be approximated. Before doing so, one has to choose whether pointwise values or cell-averaged values of u are used. The pointwise value u_i, for instance, can be defined, in the center of the cell i. The cell-averaged value of cell i, which will be denoted $\bar{u}_i$ can be defined as

$$\bar{u}_i = \frac{1}{\Delta x}\int_{x_{i-1/2}}^{x_{i+1/2}} u(x)\,\mathrm{d}x. \tag{5}$$

Note the use of the notation $\bar{u}_i$ indicating a cell-averaged value, as opposed to u_i indicating the pointwise value of 'u' in the cell center.

In a "pointwise" approach, a scheme of high-order accuracy in space does not only require the fluxes to be approximated with high-order accuracy but also the integral (appearing after the time derivative). One, therefore, needs a high-order quadrature formula for the calculation of the integral. Note that strictly speaking the latter is only necessary for high-order spatial accuracy in unsteady calculations. In steady calculations, the time derivatives vanish and the spatial accuracy only depends on the accuracy with which the cell face fluxes are approximated.

In a "cell-averaged" approach, the integral does not have to be evaluated since its value is stored (it is the cell-averaged value) and Eq. (4) is simplified to

$$\frac{\partial \bar{u}_i}{\partial t}\Delta x + f_{i+1/2} - f_{i-1/2} = 0. \tag{6}$$

This approach seems therefore preferable, since both for unsteady and steady problems, a high-order spatial accuracy is guaranteed by using a high-order approximation for the cell face fluxes. For this reason, the cell-averaged approach will be assumed in the remainder of this paper. Note that the use of cell-averaged values was already advocated by Kobayashi [17].

Next, the fluxes $f_{i+1/2}$ and $f_{i-1/2}$ have to be evaluated.

Since the relation between f and u is known, this reduces to the problem of evaluating $u_{i+1/2}$ and $u_{i-1/2}$, i.e., the value of the unknowns at the cell faces. In classical schemes, such as the second-order central or MUSCL type schemes, an explicit formula is used to obtain cell face values from cell centered values. Here, an approach based on an implicit interpolation formula is proposed [18,21]:

$$\beta u_{i-3/2} + \alpha u_{i-1/2} + u_{i+1/2} + \alpha u_{i+3/2} + \beta u_{i+5/2} = a\frac{\bar{u}_{i+1} + \bar{u}_i}{2} + b\frac{\bar{u}_{i+2} + \bar{u}_{i-1}}{2} + c\frac{\bar{u}_{i+3} + \bar{u}_{i-2}}{2}. \tag{7}$$

Note that the unknowns in the right-hand side are the cell-averaged values as defined in Eq. (5). The reason for this implicit step is that one can easily achieve high orders of accuracy with relatively small stencils. Note also the resemblance with the implicit step of the Padé type schemes, Eq. (1). This is also the approach proposed in [17] and, in a slightly different formulation, also in [16].

The coefficients a, b, c, and α, β in (7) can be derived by developing all the variables in a Taylor series about point $i + 1/2$ and requiring all the coefficients of the resulting expansion to vanish up to some definite term. For the cell-averaged values in the right-hand side, the Taylor series have to be integrated over the cells. Consider as an example the term $\bar{u}_{i+2}$. Taylor expansion of the pointwise value u around point $i + 1/2$ gives:

$$u = u_{i+1/2} + \left.\frac{\partial u}{\partial x}\right|_{i+1/2} x + \frac{1}{2}\left.\frac{\partial^2 u}{\partial x^2}\right|_{i+1/2} x^2 + \mathrm{HOT}, \tag{8}$$

where HOT stands for 'higher-order terms' and the x-coordinate has its origin in point $i + 1/2$. Inserting this expansion in the definition of $\bar{u}_{i+2}$, (5), one obtains

$$\bar{u}_{i+2} = \frac{1}{\Delta x}\int_{x_{i+3/2}}^{x_{i+5/2}} u(x)\,\mathrm{d}x = u_{i+1/2} + \frac{3}{2}\Delta x\left.\frac{\partial u}{\partial x}\right|_{i+1/2} + \frac{7}{6}\Delta x^2\left.\frac{\partial^2 u}{\partial x^2}\right|_{i+1/2} + \mathrm{HOT}. \tag{9}$$

A similar approach is used for the remaining terms in the right-hand side, whereas a regular Taylor expansion can be used for the pointwise value appearing in the left-hand side of (7). By equating terms of the same order in Δx in the left- and right-hand side, the order of the interpolation is chosen. This leads to the following results. The approximation is second-order accurate provided the following relation is satisfied:

$$a + b + c = 1 + 2\alpha + 2\beta. \tag{10}$$

For higher-order accuracy, additional relations have to be fulfilled.

For fourth order:

$$a + (2^3 - 1)b + (3^3 - 2^3)c = 2\tfrac{3!}{2!}(\alpha + 2^2\beta). \tag{11}$$

For sixth order:

$$a + (2^5 - 1)b + (3^5 - 2^5)c = 2\tfrac{5!}{4!}(\alpha + 2^4\beta). \tag{12}$$

For eighth order:

$$a + (2^7 - 1)b + (3^7 - 2^7)c = 2\tfrac{7!}{6!}(\alpha + 2^6\beta). \tag{13}$$

For 10th order:

$$a + (2^9 - 1)b + (3^9 - 2^9)c = 2\tfrac{9!}{8!}(\alpha + 2^8\beta). \tag{14}$$

For example, for fourth order, assuming $\beta = b = c = 0$, one obtains from (10) and (11):

$$\tfrac{1}{4}u_{i-1/2} + u_{i+1/2} + \tfrac{1}{4}u_{i+3/2} = \tfrac{3}{4}\left(\bar{u}_{i+1} + \bar{u}_i\right). \tag{15}$$

It is important to note that the conditions above will be different if pointwise unknowns instead of cell-averaged unknowns are used. For example, instead of (15), one obtains the following fourth-order interpolation formula (on uniform grids), [1]:

$$\tfrac{1}{6}u_{i-1/2} + u_{i+1/2} + \tfrac{1}{6}u_{i+3/2} = \tfrac{2}{3}(u_{i+1} + u_i). \tag{16}$$

It can easily be verified that for linear convection, on a uniform grid, the resulting scheme is identical to the compact Finite Difference schemes formulated in [1]. Assuming linear convection with speed $a = 1$

$$\frac{\partial u}{\partial t} + \frac{\partial u}{\partial x} = 0, \tag{17}$$

the present approach leads to

$$\frac{\partial \bar{u}_i}{\partial t} + \left.\frac{\Delta u}{\Delta x}\right|_i = 0. \tag{18}$$

With

$$\left.\frac{\Delta u}{\Delta x}\right|_i \equiv \frac{u_{i+1/2} - u_{i-1/2}}{\Delta x}, \tag{19}$$

the following equation is obtained for $\Delta u/\Delta x$ according to Eq. (7)

$$\begin{aligned}&\beta\left.\frac{\Delta u}{\Delta x}\right|_{i-2} + \alpha\left.\frac{\Delta u}{\Delta x}\right|_{i-1} + \left.\frac{\Delta u}{\Delta x}\right|_i + \alpha\left.\frac{\Delta u}{\Delta x}\right|_{i+1} + \beta\left.\frac{\Delta u}{\Delta x}\right|_{i+2}\\ &\quad= \frac{c}{2}(\bar{u}_{i+3} - \bar{u}_{i-3}) + \left(\frac{b}{2} - \frac{c}{2}\right)(\bar{u}_{i+2} - \bar{u}_{i-2}) + \left(\frac{a}{2} - \frac{b}{2}\right)(\bar{u}_{i+1} - \bar{u}_{i-1}).\end{aligned} \tag{20}$$

The Lele scheme leads to

$$\frac{\partial u_i}{\partial t} + u'_i = 0, \tag{21}$$

with u'_i satisfying Eq. (1). Comparing Eqs. (18), (20) with (21), (1) it is seen that both approaches are equivalent provided

$$c = \frac{C}{3}, \quad 2(b - c) = B, \quad a - b = A, \quad \beta = \gamma, \quad \alpha = \kappa. \tag{22}$$

Note, however, that in the Lele scheme, u_i represents a pointwise value, whereas in the present approach $\bar{u}_i$ is a cell-averaged value.

The spectral behaviour of this scheme can be studied by comparing the numerical convection speed with the actual convection speed for Fourier waves with increasing wavenumbers, e.g. [1]. The resulting plot, which can also be found in, e.g. [1] (since the present finite volume schemes are identical to their finite difference versions on uniform, 1D grids), is given here once more for completeness, Fig. 1.

The stability analysis of the resulting schemes can be found in [22], see also [1], and leads to the following condition:

$$\sigma \leqslant \frac{s}{\tilde{k}_{\max}}, \tag{23}$$

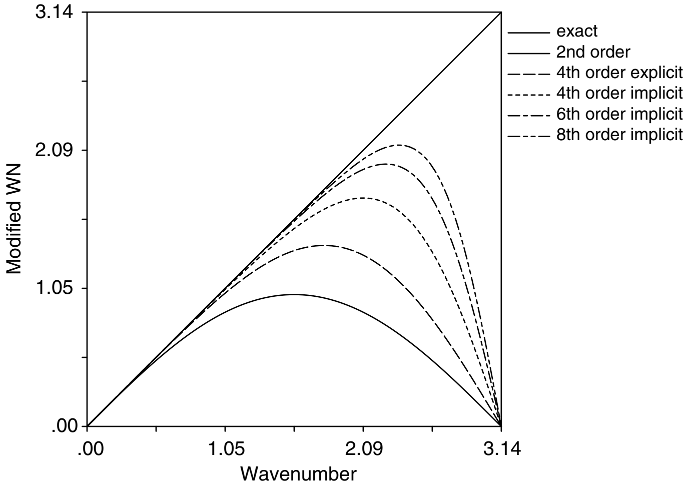

Fig. 1. Resolution of different schemes.

with σ the CFL number, 's' the segment on the imaginary axis, where the time advancement scheme is stable, and $\tilde{k}_{\max}$ the maximum modified wavenumber of the scheme, i.e., the maximum ordinate in Fig. 1. For schemes (15) and (16), one finds, resp., $\tilde{k}_{\max} = \sqrt{3}$ and $\tilde{k}_{\max} = \sqrt{2}$, as can be verified in Fig. 1. Assuming a standard fourth-order Runge–Kutta scheme (RK4) for time integration ($s = 2.85$), this leads to the following stability conditions:

$$\sigma \leqslant 1.645 \tag{24}$$

for scheme (15) and

$$\sigma \leqslant 2.015 \tag{25}$$

for scheme (16).

Two further remarks can be made here.

First, schemes with an accuracy higher than 4 can be obtained by considering a more extended stencil than (15), cf. Eq. (7). In the present paper we restrict ourselves to the former stencils, i.e., leading to tridiagonal systems and with an explicit (right-hand side) part involving only the cells in the immediate neighbourhood of the cell face. This is also advantageous for the treatment near the boundaries where in fact no special procedure is needed.

Second, the formulas above have been derived assuming uniform grids. The resulting scheme is therefore only of high-order accuracy on such grids. However, more general expressions can be derived on non-uniform grids. This will be discussed in Section 3 where the extension to multidimensions is considered. The formula's developed there will reduce to their 1D counterpart on Cartesian (but not necessarily uniform grids).

For the convection equation, the spatial discretization is now complete. For example, a fourth-order accurate scheme results by writing Eq. (15) for all cell face values and solving the resulting tridiagonal system. No special treatment is needed near the boundaries. On the inlet boundary, the flux (or u) will be imposed, whereas it is extrapolated at the outlet. The cell face fluxes follow immediately from the cell face values, through the relation $f(u)$.

In the non-linear case, an alternative approach consists in first calculating cell-averaged fluxes ($\bar{f}_i$, denoted with a $^-$ superscript similar as cell-averaged values) from the cell-averaged values, followed by an interpolation, similar to (7), to get the fluxes on the cell face:

$$\beta f_{i-3/2} + \alpha f_{i-1/2} + f_{i+1/2} + \alpha f_{i+3/2} + \beta f_{i+5/2} = a\frac{\bar{f}_{i+1} + \bar{f}_i}{2} + b\frac{\bar{f}_{i+2} + \bar{f}_{i-1}}{2} + c\frac{\bar{f}_{i+3} + \bar{f}_{i-2}}{2}. \tag{26}$$

The disadvantage of this approach (in combination with cell-averaged values of u) is that the calculation of the cell-averaged flux is not straightforward. Indeed

$$\bar{f}_i \equiv \frac{1}{\Delta x}\int_{x_{i-1/2}}^{x_{i+1/2}} f\,\mathrm{d}x, \tag{27}$$

and hence the relation

$$\bar{f}_i = f(\bar{u}_i) \tag{28}$$

is not valid unless f is a linear function of u. In all other cases one can show that the leading error term is of second order, i.e.,

$$\bar{f}_i = f(\bar{u}_i) + \mathrm{O}(\Delta x^2), \tag{29}$$

reducing the resulting scheme to second-order accuracy. An alternative route would be to calculate pointwise fluxes f_i but then pointwise values u_i are needed and these are not available. Therefore, this approach will not be used.

3. Finite volume compact schemes in multidimensions: the linear case

Now let us consider the linear 2D scalar advection equation

$$u_t + f_x + g_y = 0, \tag{30}$$

where $f = au$ and $g = bu$, a and b being constants.

Consider the structured mesh of Fig. 2. Note that the mesh does not have to be Cartesian. Integrating Eq. (30) over the cells and making use of the Gauss theorem, one can write

$$\int\int_{\Omega_{i,j}} \frac{\partial u}{\partial t}\,\mathrm{d}x\,\mathrm{d}y + \oint_{ABB'A'A} (-g\,\mathrm{d}x + f\,\mathrm{d}y) = 0, \tag{31}$$

with $\Omega_{i,j}$ the cell volume (or cell area in 2D).

To discretize this equation, both surface and line integrals must be approximated. Before doing this, as for the 1D case described above, one has to choose whether point-wise or cell-averaged values of u will be used. For the reasons mentioned above, again the cell-averaged approach is chosen. Eq. (31) reduces to (assuming a fixed grid, i.e., $\Omega_{i,j}$ does not change with time)

$$\Omega_{ij}\frac{\partial}{\partial t}\bar{u}_{i,j} + \oint_{ABB'A'A} (-g\,\mathrm{d}x + f\,\mathrm{d}y) = 0, \tag{32}$$

with $\bar{u}_{i,j}$ the cell-averaged value, i.e.,

$$\bar{u}_{i,j} \equiv \frac{1}{\Omega_{i,j}}\int\int_{\Omega_{i,j}} u(x,y)\,\mathrm{d}x\,\mathrm{d}y. \tag{33}$$

In contrast with the 1D case, where the cell face fluxes appeared after integrating over the cell volume, now *line integrals* of the fluxes appear. This complicates matters, compared to the 1D case. If one would try a similar approach, calculating face values of the unknowns, one has to make sure that the line integral of the

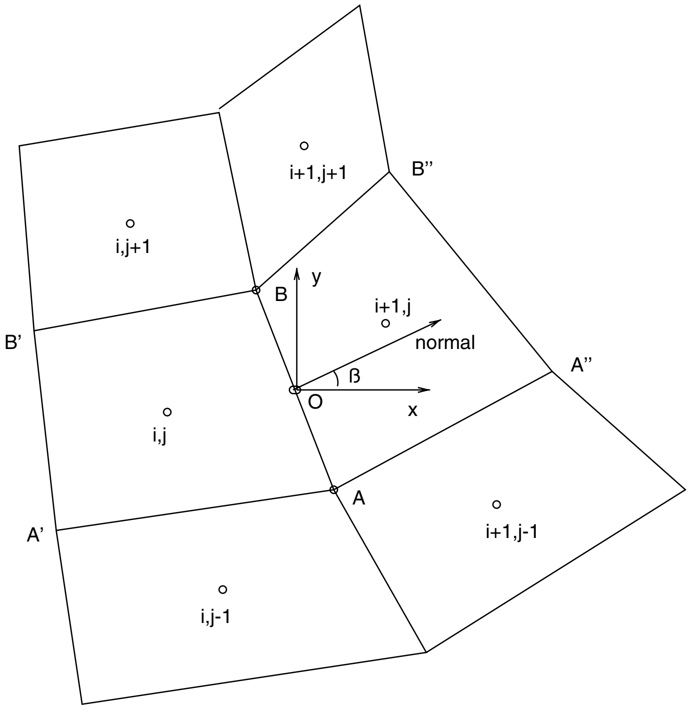

Fig. 2. Part of an arbitrary, 2D structured mesh.

flux is calculated from these values with enough accuracy. This would be possible with Gauss integration but would require face values of 'u' in the different Gauss points. Therefore, a more direct approach is proposed, where, instead of passing via cell face values of u, the line integrals itself are directly calculated [18]. A similar approach was independently proposed by Pereira et al. [19,20].

As all the integrals are approximated in the same manner, we only consider $\int_A^B f\,\mathrm{d}y$. Also note that, due to the assumption of linearity, the integrals of the fluxes reduce to integral of the unknown 'u', i.e., $\int_A^B u\,\mathrm{d}y$ in the present example. Following the strategy of constructing the Padé type schemes, the idea is to use an implicit formula for evaluating the line integrals over the cell faces.

First, assume that the grid is Cartesian and uniform. Once the cell-averaged values of u are given in the cells, one can calculate the line integral $\tilde{u} \equiv \int_A^B u\,\mathrm{d}y$ by means of, e.g., the following implicit formula, cf. Eq. (15)

$$\tfrac{1}{4}\tilde{u}_{i-1/2,j} + \tilde{u}_{i+1/2,j} + \tfrac{1}{4}\tilde{u}_{i+3/2,j} == \tfrac{3}{4}\Big(\bar{u}_{i+1,j} + \bar{u}_{i,j}\Big), \tag{34}$$

where the operator $^{-}$ indicates, as before, cell-averaged values and the operator $^{\sim}$ a value integrated over a cell face (i.e., a line integral)

$$\begin{aligned} \tilde{u}_{i-1/2,j} &= \frac{1}{y_{B'} - y_{A'}} \int_{A'}^{B'} u\,\mathrm{d}y, \\ \tilde{u}_{i+1/2,j} &= \frac{1}{y_B - y_A} \int_{A}^{B} u\,\mathrm{d}y, \\ \tilde{u}_{i+3/2,j} &= \frac{1}{y_{B''} - y_{A''}} \int_{A''}^{B''} u\,\mathrm{d}y. \end{aligned} \tag{35}$$

It can be easily shown that (34) is fourth-order accurate on a Cartesian, uniform mesh in a similar way as was shown in 1D, i.e., by developing u in a 2D Taylor series around point $i+1/2, j$. Note that a still higher-order accuracy can be achieved by widening the stencil of Eq. (34), leading to, cf. Eq. (7):

$$\begin{aligned}&\beta\tilde{u}_{i-3/2,j}+\alpha\tilde{u}_{i-1/2,j}+\tilde{u}_{i+1/2,j}+\alpha\tilde{u}_{i+3/2,j}+\beta\tilde{u}_{i+5/2,j}\\&\quad=a\frac{\bar{u}_{i+1,j}+\bar{u}_{i,j}}{2}+b\frac{\bar{u}_{i+2,j}+\bar{u}_{i-1,j}}{2}+c\frac{\bar{u}_{i+3,j}+\bar{u}_{i-2,j}}{2}.\end{aligned}\tag{36}$$

However, if one uses the above schemes, either with Eq. (34) or Eq. (36) on general (i.e., non-Cartesian, non-uniform) meshes, the order of accuracy of the Cartesian, uniform mesh is not guaranteed anymore. Actually, it can be verified that a first-order error term appears in the expressions (34) and (36). Although the errors are small on slightly distorted meshes, in general, one may need to use a formula that takes the metrics of the grid into account.

In order to guarantee a high-order accuracy on an arbitrary grid, the stencil of Eq. (34) must be extended. For the sake of compactness, the following scheme is proposed:

$$\beta\tilde{u}_{i-1/2,j}+\tilde{u}_{i+1/2,j}+\gamma\tilde{u}_{i+3/2,j}=\sum_{n=0}^{1}\sum_{m=-1}^{1}a_{n,m}\bar{u}_{i+n,j+m}.\tag{37}$$

Coefficients $a_{n,m}$, β, γ can be chosen so that (37) has the highest accuracy possible. To fit all the coefficients of the Taylor series of both right-hand and left-hand sides of (37) up to order 4, one has to satisfy 10 relations, the details of which are given in Appendix A.

However, there are only eight coefficients in (37), which means that the linear system of equations to be solved is overdefined. Therefore, on arbitrary meshes, it is not possible to approximate $\int_A^B u\,\mathrm{d}y$ with fourth-order accuracy on the stencil given by (37). Third-order accuracy can be obtained if the first six relations ((A.2)–(A.7), cf. Appendix A) are satisfied. This leaves 2 degrees of freedom in defining the eight coefficients. This freedom can then be used to minimize the leading error term, which is of order 3 and contains the third-order derivatives with respect to x and y, as well as the mixed derivatives. The sum of the squares of the coefficients of these terms is then minimized. These coefficients are the differences between left-hand-side and right-hand side of Eqs. (A.8)–(A.11) of Appendix A. We will denote this scheme as CS3 (Compact Scheme, third order).

On Cartesian meshes (not necessarily uniform though), the leading truncation error of the CS3 scheme vanishes, making the scheme fourth-order accurate. It can also be verified from the expressions in Appendix A that the formula (37) reduces to a 1D formula (i.e., only the coefficients $a_{n,0}$, $n=0,1$ are non-zero) on a Cartesian grid. If in addition the grid is uniform, relation (34) is retrieved.

The resulting stencil on a non-uniform Cartesian grid, which is 1D as mentioned above, can then also be used for 1D convection to replace expression (15) and to guarantee fourth-order accuracy on a non-uniform 1D mesh.

Numerical tests, see Section 6, have shown however that on *very* distorted grids the third-order accurate scheme, as defined above, shows a strong oscillatory behaviour, making the calculations unstable. This could be related to a lack of diagonal dominance in Eq. (37). Since this is difficult to analyse mathematically on arbitrary grids, it was verified in a numerical experiment. It turned out that diagonal dominance was always largely satisfied.

To overcome the stability problem, a scheme with formal accuracy of one order less was constructed. β and γ were set to $1/4$ in Eq. (37), their values in the formulation for a uniform Cartesian mesh, and the remaining six coefficients $a_{n,m}$ were chosen by imposing second-order accuracy of (37). In this case only the first three constraints ((A.2)–(A.4), cf. Appendix A) have to be satisfied leaving 3 degrees of freedom. Again these are used to minimize the sum of the square of the coefficients of the leading error term (which is now of second order). These coefficients are the differences between left-hand side and right-hand side of Eqs. (A.5)–(A.7) of Appendix A. This scheme will be denoted as CS2.

As for the CS3 scheme, the CS2 scheme becomes 1D on Cartesian grids. If the grid is uniform, fourth-order accuracy is achieved. If the Cartesian grid is non-uniform, the CS2 scheme reduces to a second-order accurate scheme, as on arbitrary grids. Note that this is in contrast with the CS3 scheme which guarantees fourth-order accuracy on all Cartesian grids, uniform or non-uniform.

Although, the formal order of accuracy of the proposed scheme is only 2 (except on Cartesian, uniform grids where it is 4), this order is guaranteed on arbitrary grids, whereas the order of the standard central scheme is much less than 2 on such grids. In addition one has to make the distinction between the order of approximation of a scheme, as based on a Taylor expansion, and the resolution of the scheme which is related to its ability to represent Fourier modes of increasing wavenumbers accurately [23]. For applications in LES, and a fortiori in DNS, the latter property becomes more important in order to simulate the different scales in the flow as accurate as possible. On Fig. 1 it can be seen that the present scheme, which reduces to the standard fourth-order compact scheme on a uniform grid in 1D, behaves much better than the standard second-order central scheme, especially for the higher wavenumbers. This will also be confirmed in the numerical tests presented in Section 6.

The procedure described above can now be repeated for all integrals of 'u' along the cell faces, making the discretization of Eq. (32) (in this linear case) complete.

4. Finite volume compact schemes for the Navier–Stokes system

Now, consider the 2D Navier–Stokes system written in the form

$$\frac{\partial U}{\partial t}+\frac{\partial F_x}{\partial x}+\frac{\partial F_y}{\partial y}=\frac{\partial G_x}{\partial x}+\frac{\partial G_y}{\partial y}, \tag{38}$$

where U is the set of conservative variables and F_x, F_y and G_x, G_y are components of the advective and diffusive flux vectors, respectively:

$$U=\begin{pmatrix}\rho\\ \rho u\\ \rho v\\ \rho E\end{pmatrix}, \tag{39}$$

$$F_x=\begin{pmatrix}\rho u\\ \rho u^2+p\\ \rho uv\\ (\rho E+p)u\end{pmatrix},\quad F_y=\begin{pmatrix}\rho v\\ \rho uv\\ \rho v^2+p\\ (\rho E+p)v\end{pmatrix}, \tag{40}$$

with ρ, u, v, p, E, respectively, density, x, and y components of velocity, pressure, and total energy per unit mass.

As in the previous section, consider the structured, arbitrary mesh of Fig. 2. Integrating Eq. (38) over the cells and making use of the Gauss theorem, one can write

$$\int\int_{\Omega_{i,j}}\frac{\partial U}{\partial t}\,\mathrm{d}x\,\mathrm{d}y+\oint_{ABB'A'A}(-F_y\,\mathrm{d}x+F_x\,\mathrm{d}y)=\oint_{ABB'A'A}(-G_y\,\mathrm{d}x+G_x\,\mathrm{d}y). \tag{41}$$

For the reasons explained before, it is chosen to store cell-averaged values of the unknowns, instead of pointwise. Since in the present code the primitive variables $V \equiv (\rho, u, v, p)$ are stored, the cell-averaged values of these variables will be used. Again, we use the notation $^{-}$ to indicate a cell-averaged variable and $\bar{V}$ is therefore shorthand notation for the cell-averaged primitive variables:

$$\bar{V} = \begin{pmatrix} \bar{\rho} \\ \bar{u} \\ \bar{v} \\ \bar{p} \end{pmatrix}. \tag{42}$$

Let us now consider the discretization of the line integrals in (41) and first focus on the convective terms.

4.1. Compact scheme for the convective terms

As all the integrals are approximated in the same manner, we will only consider $\int_A^B F_x \, \mathrm{d}y$. As opposed to the previous section, the fluxes are now non-linear functions of the unknowns (primitive variables). The proposed scheme consists of two steps.

The first step is similar as for the linear case: the integrals along the cell faces of the primitive variables are approximated using an implicit formulation, similar as in Eq. (37). In shorthand notation:

$$\beta \tilde{V}_{i-1/2,j} + \tilde{V}_{i+1/2,j} + \gamma \tilde{V}_{i+3/2,j} = \sum_{n=0}^{1} \sum_{m=-1}^{1} a_{n,m} \bar{V}_{i+n,j+m}, \tag{43}$$

where

$$\begin{aligned} \tilde{V}_{i-1/2,j} &= \frac{1}{y_{B'} - y_{A'}} \int_{A'}^{B'} V \, \mathrm{d}y, \\ \tilde{V}_{i+1/2,j} &= \frac{1}{y_B - y_A} \int_A^B V \, \mathrm{d}y, \\ \tilde{V}_{i+3/2,j} &= \frac{1}{y_{B''} - y_{A''}} \int_{A''}^{B''} V \, \mathrm{d}y. \end{aligned} \tag{44}$$

The coefficients of this interpolation are only geometry-dependent and therefore identical to those derived for the linear case of previous section. Again, the third-order accurate scheme shows an oscillatory behaviour, resulting in stability problems on very distorted grids, and the second-order accurate version is chosen.

The second step of the method consists in evaluating the integrals of the fluxes which, in contrast to the scalar convective case, contain non-linear terms, cf. the expressions for the fluxes of Eq. (40). Consider for instance the first component of F_x. The corresponding line integral is $\int_A^B \rho(x,y)u(x,y) \, \mathrm{d}y$. The following formula may be used to approximate this integral:

$$\frac{1}{y_B - y_A} \int_A^B \rho u \, \mathrm{d}y \approx \frac{1}{y_B - y_A} \int_A^B \rho \, \mathrm{d}y \frac{1}{y_B - y_A} \int_A^B u \, \mathrm{d}y. \tag{45}$$

If one works out both sides of this equation, using Taylor expansions around the cell face center (e.g., point O for face $i + 1/2, j$ in Fig. 2), it appears that the above approximation introduces an error term of order 2. Using shorthand notation, the correct relation is

$$\widetilde{\rho u}_{i+1/2,j} = \tilde{\rho}_{i+1/2,j} \tilde{u}_{i+1/2,j} + \rho'_x u'_x \frac{\Delta x^2}{12} + \rho'_y u'_y \frac{\Delta y^2}{12} + (\rho'_x u'_y + \rho'_y u'_x) \frac{\Delta x \Delta y}{12} + \mathrm{O}(h^4), \tag{46}$$

where $'$ indicates the first-order derivative in point O. The leading truncation error is thus of order 2, assuming that the derivatives of the variables do not vanish (if this is the case it means that ρ and u are constant and the complete error term in relation (46) vanishes). A similar relation was used by Pereira et al. [19,20]. Since they work in computational space, a simplified relation can be used valid on Cartesian grids.

If one only aims at a second-order accurate scheme (irrespective whether the grid is Cartesian or not) relations of type (45) can be used without any further correction. First, the line integrals of the primitive variables along the cell faces are evaluated using Eq. (43). Next relations of type (45) are used to evaluate the line integrals of the different components of the fluxes. The resulting scheme will be second-order accurate on any mesh.

If one wants to retrieve a fourth-order accurate scheme on Cartesian grids, relation (46) instead of (45) has to be used. If the derivatives are approximated with second-order accuracy the resulting approximation becomes fourth-order accurate. The derivatives ρ'_x, u'_x, ρ'_y, u'_y in (46) are calculated as an average of two cell-averaged values of derivatives in cells next to the interface. For example (cf. Fig. 2):

$$u'_x\big|_{i+1/2,j} = \frac{1}{2}\left(\left.\overline{\frac{\partial u}{\partial x}}\right|_{i+1,j} + \left.\overline{\frac{\partial u}{\partial x}}\right|_{i,j}\right). \tag{47}$$

Cell-averaged values of derivatives are calculated by means of the finite volume method (cf. Fig. 2):

$$\left.\overline{\frac{\partial u}{\partial x}}\right|_{i,j} = \frac{1}{\Omega_{i,j}}\left[\widetilde{u}_{i+1/2,j}(y_B - y_A) - \widetilde{u}_{i-1/2,j}(y_{B'} - y_{A'}) + \widetilde{u}_{i,j+1/2}(y_{B'} - y_B) - \widetilde{u}_{i,j-1/2}(y_{A'} - y_A)\right]. \tag{48}$$

Note that $\widetilde{u}_{i+1/2,j}$, etc., have already been calculated by (43).

The same procedure can also be used for the flux components depending on three variables, e.g., second component of F_y. One can show that

$$\begin{aligned}\widetilde{\rho u v} = {} & \tilde{\rho}\cdot\tilde{u}\cdot\tilde{v} + +(\rho'_x u'_x v_O + \rho'_x u_O v'_x + \rho_O u'_x v'_x)\frac{\Delta x^2}{12} + (\rho'_y u'_y v_O + \rho'_y u_O v'_y + \rho_O u'_y v'_y)\frac{\Delta y^2}{12} \\ & + \left[(\rho'_x u_y + \rho'_y u_x)v_O + (\rho'_x v_y + \rho'_y v_x)u_O + (u'_x v_y + u'_y v_x)\rho_O\right]\frac{\Delta x \Delta y}{12} + O(h^4).\end{aligned} \tag{49}$$

Apart from the derivatives ρ'_x, u'_x, v'_x, ρ'_y, u'_y, v'_y also the pointwise values ρ_O, u_O, v_O now have to be approximated with second-order accuracy. The following formula is used, e.g., for u_O:

$$u_O = \frac{\overline{u}_{i+1,j} + \overline{u}_{i,j}}{2}. \tag{50}$$

The approach above allows to calculate all flux integrals with second-order accuracy on arbitrary grids and fourth-order accuracy on Cartesian, uniform grids. This completes the scheme for the convective terms of the Navier–Stokes equations. Note that because of the use of tridiagonal systems, cf. Eq. (43), no special procedure near the boundaries is needed. Equations of type (43) can be written for all cell faces, except those on the boundaries. On the latter faces, the flux is determined by the boundary conditions.

4.2. Compact schemes for the viscous terms

The discretization of the viscous fluxes corresponds to the evaluation of the right-hand-side term in Eq. (41). Since the viscous fluxes contain derivatives of the velocity and the temperature, one has to determine the line integrals (over the cell faces) of these derivatives with high-order accuracy.

The same procedure as for the inviscid fluxes is used. A relation similar to (43) is used, where, in the left-hand side the line integral of the derivative appears and in the right-hand side the cell averaged values of the derivative. The obtained coefficients are identical to those in Eq. (43). The cell-averaged values of the derivative are calculated as follows:

$$\overline{\left(\frac{\partial u}{\partial x}\right)}_{i,j} \equiv \frac{1}{\Omega_{i,j}} \int_{\Omega_{i,j}} \frac{\partial u}{\partial x}\,\mathrm{d}\Omega = \frac{1}{\Omega_{i,j}} \oint_{ABB'A'A} u n_x\,\mathrm{d}S = \frac{1}{\Omega_{i,j}} \oint_{ABB'A'A} u\,\mathrm{d}y. \tag{51}$$

The line integrals in (51) are already available from the discretization of the convective fluxes. Relation (51) also requires that the cell volumes are calculated with high enough accuracy. In the present application, linear elements of the serendipity family are used [24]. The volume is obtained through Gaussian quadrature with fourth-order accuracy.

The analysis of the order of accuracy leads to exactly the same coefficients (β, γ, $a_{n,m}$) as for the convective terms. Similarly as for the convective terms, a third-order accurate and a second-order accurate scheme (on arbitrary grids) can be derived for the viscous terms. In the present paper, the second-order scheme was systematically chosen for its better stability properties.

Assuming the viscosity is constant, the viscous terms are linear and a correction procedure, as applied for the convective terms, cf. Eqs. (46) and (49), is not needed. Even with a changing viscosity, and no correction procedure applied, the scheme always remains second-order accurate. This was estimated as being enough for the viscous terms and hence no correction procedure was applied.

5. Time integration

In the model problems discussed below, as well as in the Navier–Stokes applications, time-integration is performed using multistage low storage Runge–Kutta (RK) schemes:

$$U_1 = U_0 + \Delta t C_1 \mathrm{Res}(U_0), \tag{52}$$

$$U_2 = U_0 + \Delta t C_2 \mathrm{Res}(U_1), \tag{53}$$

$$\dots \tag{54}$$

$$U_N = U_0 + \Delta t C_N \mathrm{Res}(U_{N-1}), \tag{55}$$

where $\mathrm{Res}(U)$ is the residual. For linear problems with constant propagation coefficients, a Nth stage RK scheme is Nth-order accurate in time, provided the RK coefficients are chosen as follows:

$$C_k = \frac{1}{N-k+1}, \tag{56}$$

where k is the RK stage number. For non-linear problems, however, the formal accuracy in time of the scheme is only of second order.

In all the calculations below, where the spatial accuracy of the proposed schemes are evaluated, the time step was always taken sufficiently small to ensure that the errors of time integration were much smaller than those due to the spatial discretization.

6. Numerical results

The present finite-volume formulation for compact schemes has been developed with the final aim of applying it to LES simulations of turbulence. Before any LES calculations were performed, a series of tests for a scalar model problem, a 2D Euler problem, and a laminar Navier–Stokes problem were carried out. The results will be systematically compared with those of the classical second-order central scheme (CE). In this scheme, the line integral of the unknown on the cell face is obtained as an arithmetic average of the cell-averaged values in the cells left and right of the interface, i.e., referring to Fig. 2, and using the notation of Eqs. (43) and (44):

$$\tilde{V}_{i+1/2,j} = \tfrac{1}{2}\left(\bar{V}_{i,j} + \bar{V}_{i+1,j}\right). \tag{57}$$

This allows to determine the cell face flux. Note that, since this scheme is at most second-order accurate, Eq. (45) can be used, i.e., correction (46) is not needed. This is the standard implementation of the central scheme (although there, one usually reasons in terms of pointwise values) which is used in many codes, where it is combined with second- and fourth-order dissipation terms, [25]. These dissipation terms, which are added to control stability and monotonicity, are omitted in the present implementation of the CE scheme.

6.1. Model problems

To test the present formulation of compact schemes, a series of numerical experiments has been carried out for a number of 1D and 2D advection problems

$$u_t + (au)_x + (bu)_y = 0. \tag{58}$$

In all simulations, a six-stage low storage RK scheme was used to advance in time. The RK coefficients were taken as 1/6, 1/5, 1/4, 1/3, 1/2, 1. This scheme is sixth-order accurate in time for linear problems. Since only the spatial accuracy was to be examined, the time step was taken very small to make sure that the errors, occurring due to time integration, are negligible, as compared to those arising from spatial discretization.

6.1.1. Two-dimensional Gaussian wave on a uniform and a non-uniform grid

In the first experiment, a 2D signal was propagated in a domain $-0.5 < x < 0.5$, $-0.5 < y < 0.5$. A 2D Gaussian wave of the following shape:

$$u_0(x,y) = \tfrac{1}{4}\exp\left[154.037(x^2 + y^2)\right] \tag{59}$$

was used as an initial solution, and periodic boundary conditions were imposed in both x and y directions. For each test case, the wave was propagated during 5 s with a speed given by $a = 0.8$, $b = 0.6$.

In Figs. 3–5 the results obtained on the Cartesian uniform mesh (80×80 cells) are presented. Three schemes were used: the classical second-order central scheme (CE), the present compact finite-volume scheme with non-uniform coefficients (CS2_{nu}) (using Eq. (37) as opposed to Eq. (34), and a classical fourth-order central scheme (CE4). In the present application, this latter scheme corresponds to choosing

$$\tilde{u}_{i+1/2,j} = \tfrac{7}{12}\left(\bar{u}_{i+1} + \bar{u}_i\right) - \tfrac{1}{12}\left(\bar{u}_{i+2} + \bar{u}_{i-1}\right). \tag{60}$$

Both the CS2_{nu} and CE4 scheme are fourth-order accurate on this Cartesian grid. Results with the compact scheme are in excellent agreement with the exact solution (circular isolines). The CE scheme shows important errors both in terms of location of the peak of the solution (which should be in the middle of the calculation domain) and symmetry. The quality of the CE4 results is clearly inferior to that of the CS2_{nu} results. This is explained by the better spectral behaviour of CS2_{nu}, cf. Fig. 1 (curves with long and small dashes). Note that all schemes are non-monotone and therefore produce some wiggles in the solution. The

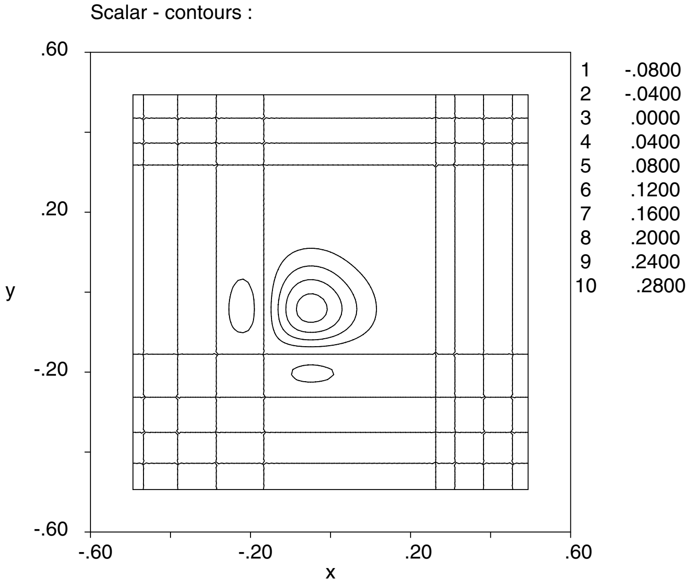

Fig. 3. Two-dimensional advection of a Gaussian wave on a Cartesian uniform grid: isolines of the solution with the CE scheme.

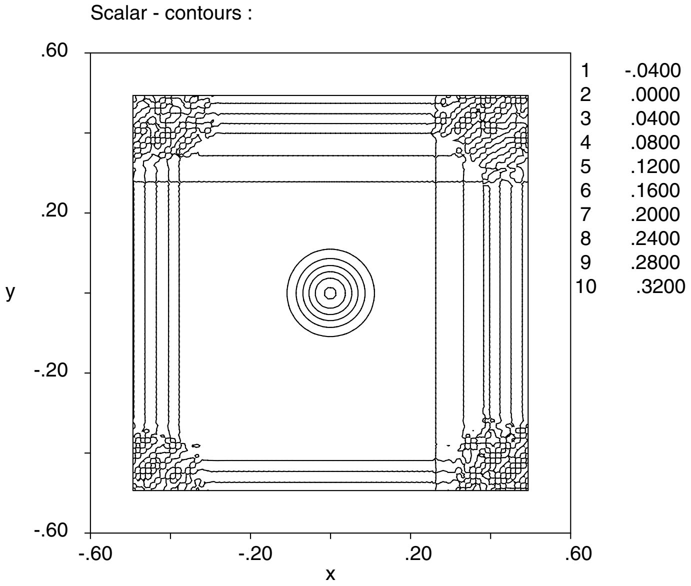

Fig. 4. Two-dimensional advection of a Gaussian wave on a Cartesian uniform grid: isolines of the solution with the $CS2_{nu}$ scheme.

oscillations of the $CS2_{nu}$ scheme, however, are very small, especially compared to those of CE, and form some 'noise' that could be removed by filtering, e.g. [12], or by adding some artificial dissipation, see also Section 6.1.3.

The previous calculations were repeated on the curvilinear mesh of Fig. 6 (80×80 cells). This mesh was obtained from the previous, Cartesian mesh by moving the mesh points according to:

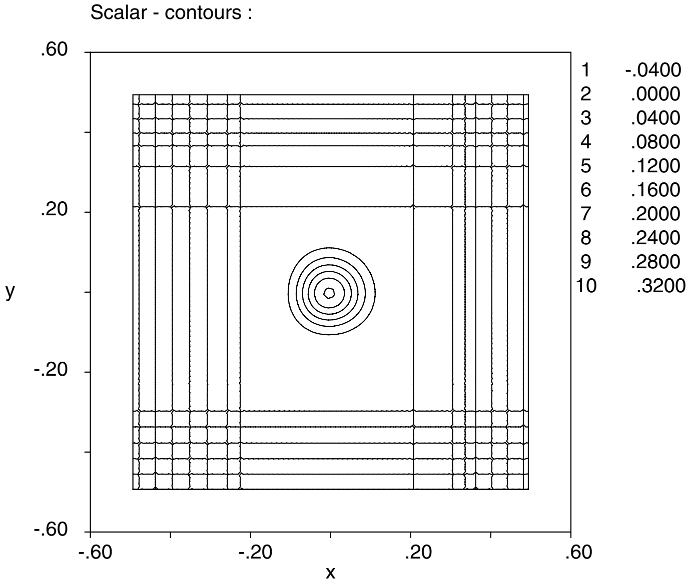

Fig. 5. Two-dimensional advection of a Gaussian wave on a Cartesian uniform grid: isolines of the solution with the CE4 scheme.

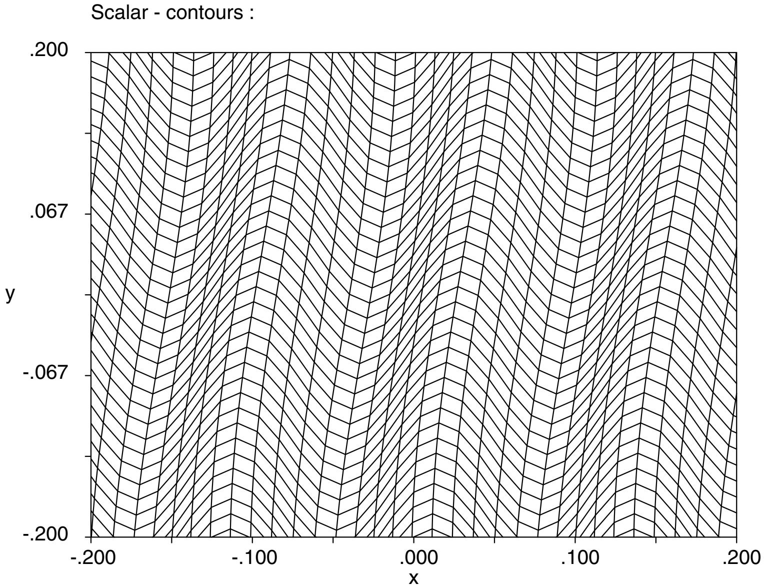

Fig. 6. Curvilinear mesh used for the 2D advection of a Gaussian wave.

$$
\begin{aligned}
x_{i,j} &= \bar{x}_{i,j} + 0.02\sin(2\pi\bar{y}_{i,j}),\\
y_{i,j} &= \bar{y}_{i,j} + 0.04\sin(16\pi\bar{x}_{i,j}),
\end{aligned}
\tag{61}
$$

with $\bar{x}_{i,j}$, $\bar{y}_{i,j}$ the coordinates of the uniform mesh. The aim of the present test is to investigate the effect of using a compact scheme with uniform coefficients ($\mathrm{CS2_u}$) as compared to one with non-uniform coefficients, $\mathrm{CS2_{nu}}$ (used in the previous test). Fig. 7 shows isolines of the solution obtained with both schemes. For

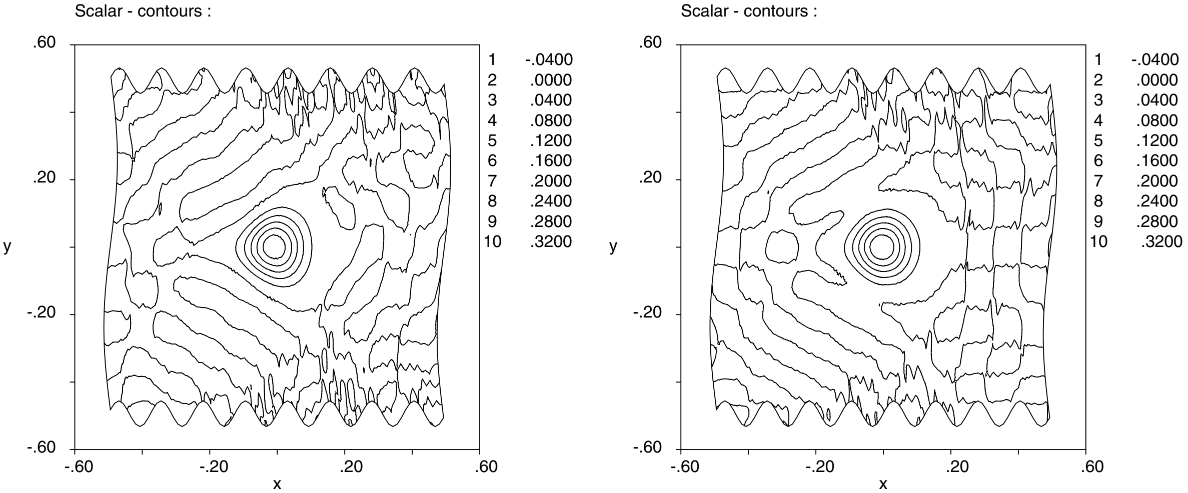

Fig. 7. Two-dimensional advection of a Gaussian wave on a curvilinear grid: isolines of the solution with the $CS2_u$ scheme (left) and $CS2_{nu}$ scheme (right).

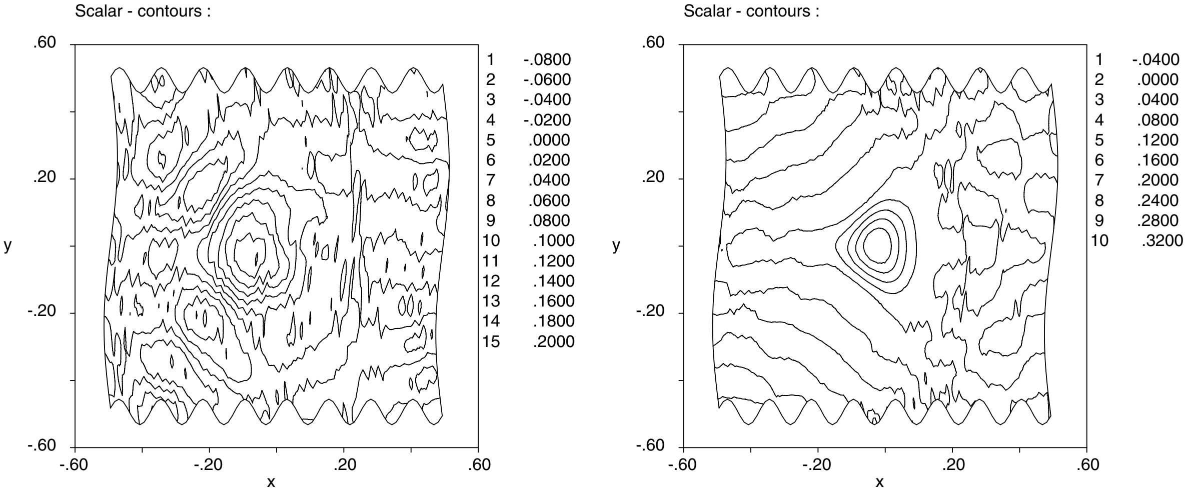

Fig. 8. Two-dimensional advection of a Gaussian wave on a curvilinear grid: isolines of the solution with the CE scheme (left) and the CE4 scheme (right).

comparison the isolines obtained with the CE and CE4 scheme are given in Fig. 8. The improvement in accuracy with the $CS2_{nu}$ scheme is visible from the isoline plot. Theoretically the $CS2_{nu}$ scheme should be second-order accurate on this mesh, whereas the $CS2_u$ will be less than second-order accurate. Also note that both $CS2_{nu}$, $CS2_u$ solutions are superior to the CE4 solution.

An analysis of the order of accuracy and the absolute error on a sequence of meshes with different levels of resolution is provided in Fig. 9. The measured order of accuracy for both schemes is, in contrast with what one would expect theoretically, 4. This can be explained by the smoothness of the grid, which, being refined, locally becomes straight and uniform, although non-orthognal. Nevertheless, the absolute error is smaller (by approximately a factor of 2) for the $CS2_{nu}$ scheme.

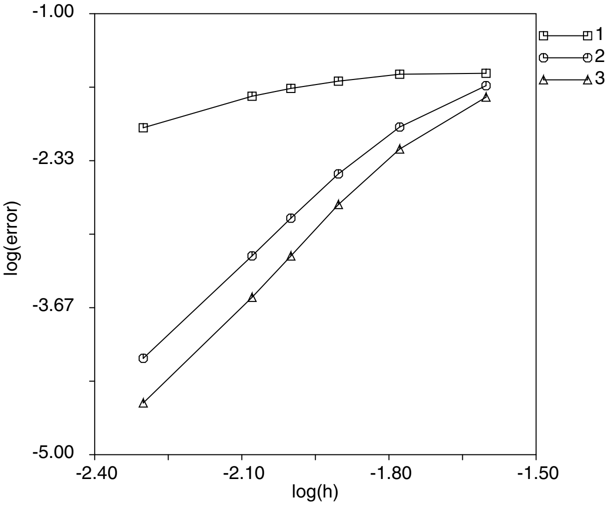

Fig. 9. Two-dimensional advection of a Gaussian wave on a curvilinear grid: grid refinement study of the mean error: 1, CE scheme; 2, $CS2_u$ scheme; 3, $CS2_{nu}$ scheme.

6.1.2. One-dimensional Gaussian wave on a non-uniform grid

To show the importance of accounting for the non-uniformity of the mesh, a 1D test case (propagation of a Gaussian wave for 1 s) was calculated on a non-uniform grid consisting of alternating bigger and smaller cells with the size ratio 11/9. Periodic boundary conditions were imposed. The 1D version of the $CS2_{nu}$ and $CS2_u$ schemes of the previous test are compared. Fig. 10 shows the results obtained with both schemes. It is seen that, in spite of the relatively small non-uniformity, the $CS2_u$ scheme shows some errors both with respect to the wave speed and the wave amplitude.

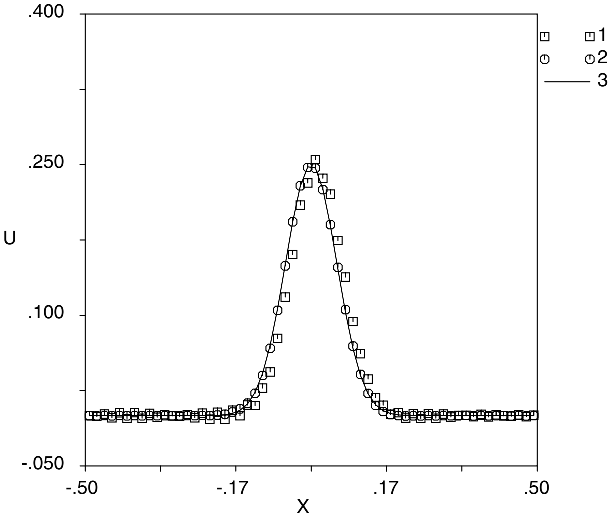

Fig. 10. One-dimensional advection of a Gaussian wave on a mesh with cell size ratio 11/9: 1, $CS2_u$ scheme; 2, $CS2_{nu}$ scheme; 3, exact solution.

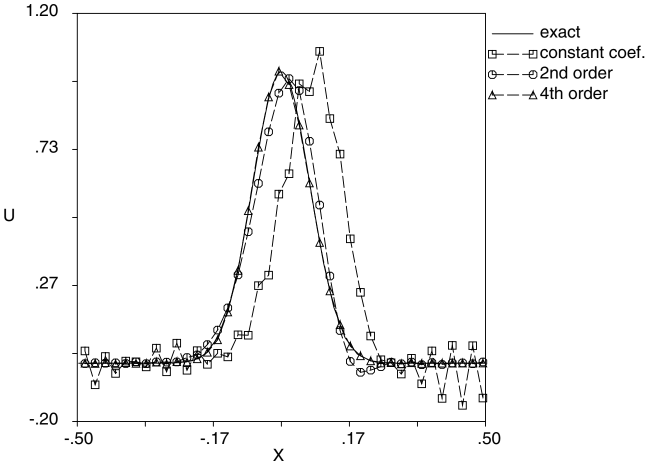

Fig. 11. One-dimensional advection of a Gaussian wave on a mesh with cell size ratio 3: squares, $CS2_u$ scheme; circles, $CS2_{nu}$ scheme; triangles, $CS3_{nu}$ scheme.

The same test case was repeated for a mesh with cell size ratio of 3. The $CS2_{nu}$ scheme is now also compared to the compact scheme $CS3_{nu}$, Fig. 11. The latter scheme is fourth-order accurate on this mesh, whereas the former only second order. The improvement is clearly visible.

6.1.3. Rotating Gaussian wave

A Gaussian wave rotating around the origin $x = 0$, $y = 0$ is described by Eq. (58) with $a = -2\pi y$, $b = 2\pi x$ (varying advection coefficients). The grid used in all calculations is an "O" type grid. In circumferential direction, periodicity is assumed, while at the inner and outer boundaries the solution is put to zero.

Note that, since the convection coefficients are not constant anymore, the use of a formula such as

$$\frac{1}{y_B - y_A}\int_A^B au\,\mathrm{d}y = \frac{1}{y_B - y_A}\int_A^B a\,\mathrm{d}y\frac{1}{y_B - y_A}\int_A^B u\,\mathrm{d}y \tag{62}$$

introduces a second-order error and makes the global scheme second-order accurate. Therefore, in contrast to the previous tests, a correction, as proposed in Eq. (46), has to be used to reduce the error in the above relation to fourth-order. The corresponding scheme is therefore denoted as $CS2^c_{nu}$, where the superscript 'c' indicates that the correction is added to the relation above (the 'nu' subscript indicates the use of non-uniform coefficients as before). To show the importance of this correction, simulations were also made with a compact scheme with no corrections (i.e., relation (62) is used), which is denoted as $CS2^{nc}_{nu}$ scheme.

The isolines of the solution after one rotation of the signal are presented in Fig. 12 for both the classical central scheme (CE) and $CS2^c_{nu}$.

Note that in the CE scheme, no artificial dissipation was used. The CE scheme is second-order accurate on uniform Cartesian grids, but on distorted meshes the accuracy is less. The $CS2^c_{nu}$ scheme is second-order accurate on arbitrary meshes, but becomes fourth-order accurate on a Cartesian mesh. Hence, if the mesh is not too irregular, the accuracy of this scheme will be close to fourth order.

A significant improvement in accuracy for the compact scheme is clearly seen. The isolines of the exact solution correspond to circular contours, which are much better approximated by the compact approach.

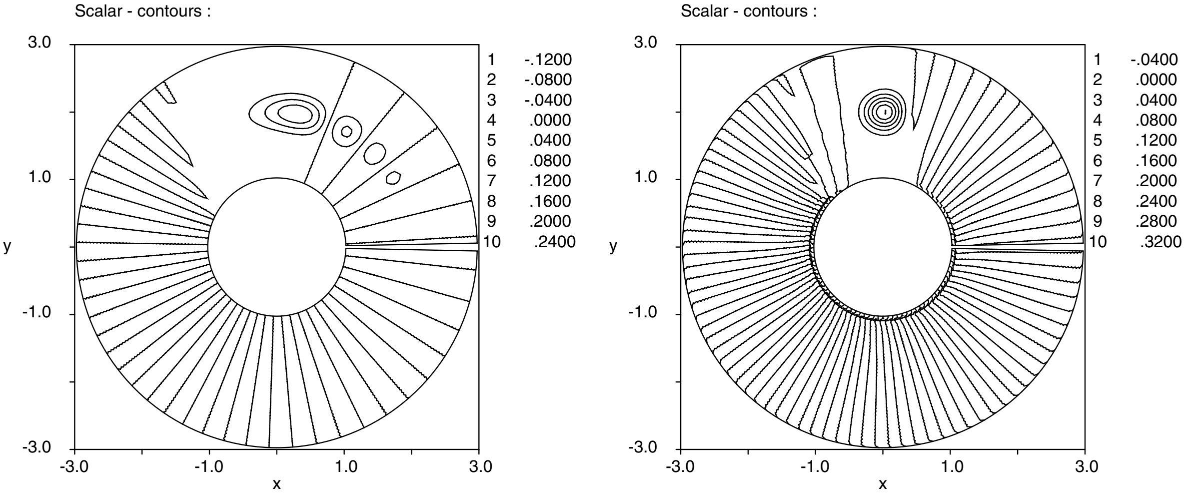

Fig. 12. Two-dimensional rotation of a Gaussian wave: isolines of the solution with the CE scheme (left) and $CS2^c_{nu}$ scheme (right) after 1 rotation.

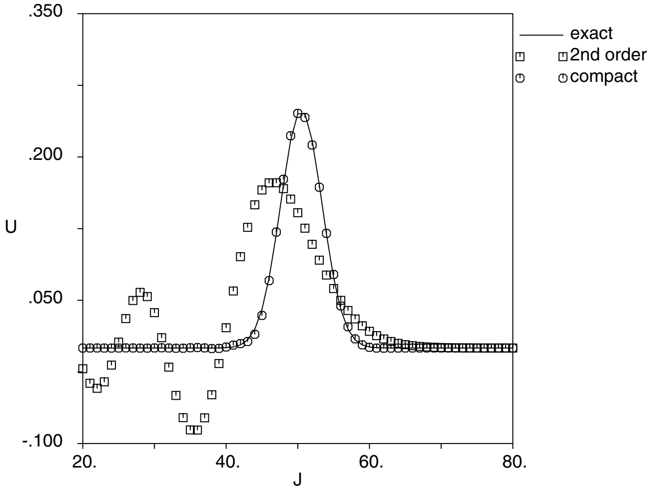

Fig. 13. Two-dimensional rotation of a Gaussian wave: solution along the circular grid line passing through the center of the Gaussian wave after 1 rotation (squares, CE scheme; circles, $CS2^c_{nu}$) scheme.

Note again the ‘noise’ in the solution due to the non-monotonicity of the schemes. The amplitude of the wiggles is much less for the compact scheme, as shown in Fig. 13, which plots the solution along a circumferential line through the center of the Gaussian wave. Note also the effect of the dispersive error of the CE scheme causing the numerical solution to lag behind the physical solution. The third-order accurate compact scheme $CS3^c_{nu}$ was also tried for this test case. It gave almost identical results as $CS2^c_{nu}$, and the solution is therefore not shown.

Fig. 14 shows the solution along the circumferential line through the center of the Gaussian wave of the $CS2^c_{nu}$ and CE scheme after 10 rotations. The results of the former scheme are still quite good (although the

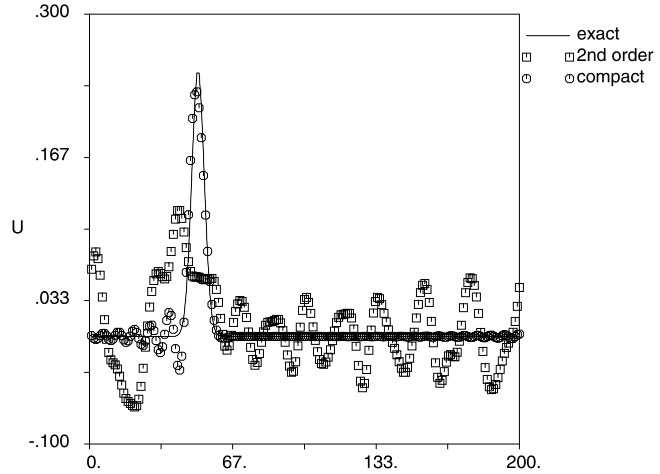

Fig. 14. Two-dimensional rotation of a Gaussian wave: solution along the circular grid line passing through the center of the Gaussian wave after 10 rotations (squares, CE scheme; circles, $CS2^{c}_{nu}$) scheme.

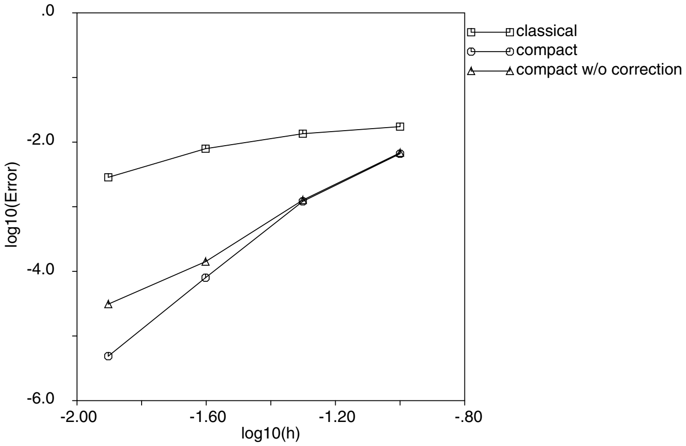

Fig. 15. Two-dimensional rotation of a Gaussian wave: grid refinement study of the mean error (squares, CE scheme; circles, $CS2^{c}_{nu}$ scheme; triangles, $CS2^{nc}_{nu}$ scheme).

oscillations have increased), whereas in the results of the latter scheme the Gaussian wave can hardly be recognized.

It is to be noted that after a sufficiently long integration time (about 50 rotations for this particular test case), during which the oscillations of the $CS2^{c}_{nu}$ scheme can build up, the simulation starts to diverge. To avoid this, some filtering procedure could be used or some artificial dissipation could be added. A formulation based on artificial selective damping, e.g. [26], is currently being investigated [27].

The achieved order of accuracy is studied numerically by calculations on a range of grids with decreasing mesh size. The results are shown in Fig. 15, where the logarithm of the mean error is plotted as a function of the logarithm of the mesh size. In this plot, results for the $CS2^{nc}_{nu}$ scheme are also included. It can be seen that the $CS2^{nc}_{nu}$ fails to maintain fourth-order accuracy. The $CS2^{c}_{nu}$ scheme seems fourth-order accurate, although theoretically it should only be second-order accurate on this non-Cartesian grid. The explanation is that the present mesh locally becomes uniform and Cartesian when refined, and therefore the measured order of accuracy is the same as the order obtained on Cartesian meshes. For the same reason the $\mathrm{CS3}^{\mathrm{c}}_{\mathrm{nu}}$ scheme is also fourth-order accurate (not shown).

6.2. Two-dimensional laminar flat Plate

The flat plate boundary layer problem is considered next. The flow was calculated with both CE and $\mathrm{CS2}^{\mathrm{c}}_{\mathrm{nu}}$ scheme on a relatively coarse mesh (100 × 25). The Blasius solution was used as an inlet boundary condition as well as a reference solution. The inlet and outlet were located in cross-sections corresponding to Reynolds numbers $Re_x = 1600$ and 11,600 based on distance from the leading edge. Figs. 16 and 17 show the profiles of non-dimensional streamwise and normal components of velocity

$$u^* \equiv \frac{u}{u_0}, \quad v^* \equiv \frac{v}{(\nu u_0/x)^{1/2}} \tag{63}$$

(where u_0 is a freestream velocity) as a function of the similarity variable

$$\eta = \frac{y}{(\nu x/u_0)^{1/2}}. \tag{64}$$

The computed velocity profiles are presented in the cross-sections corresponding to the Reynolds number $Re_x = 9600$. The CE scheme produces poor results, while the results obtained with the $\mathrm{CS2}^{\mathrm{c}}_{\mathrm{nu}}$ scheme are in good agreement with the Blasius solution.

6.3. Two-dimensional Subsonic vortical flow

The capability of the numerical schemes to accurately advect vortical structures is an important issue in DNS and LES of turbulence. Therefore, one of the problems chosen to demonstrate the accuracy of the proposed high-order compact method was a subsonic inviscid vortical flow, see also [10,19]. A vortex is

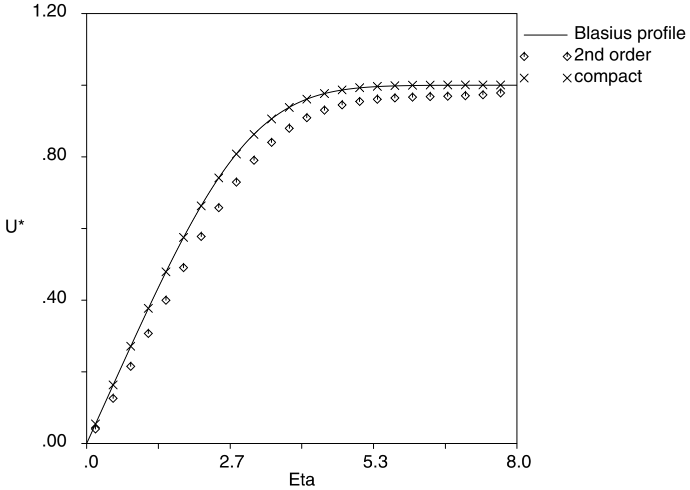

Fig. 16. Two-dimensional flat plate laminar boundary layer: streamwise component of velocity as a function of similarity variable ($Re_x = 9600$).

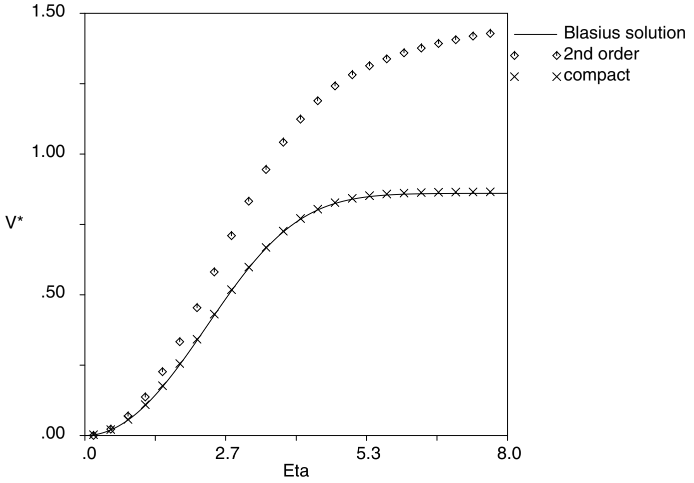

Fig. 17. Two-dimensional flat plate laminar boundary layer: normal component of velocity as a function of similarity variable ($Re_x = 9600$).

convected in otherwise uniform flow with freestream velocity $U_\infty = 10$ m/s. The initial solution is imposed by prescribing a vortical structure centered around $x = 0,\ y = 0$ as follows:

$$\begin{aligned} u &= U_\infty - \frac{Cy}{R^2}\exp(-r^2/2), \\ v &= \frac{Cx}{R^2}\exp(-r^2/2), \\ p &= P_\infty - \frac{\rho C^2}{2R^2}\exp(-r^2), \quad r = \sqrt{\frac{x^2+y^2}{R^2}}. \end{aligned} \tag{65}$$

The vortex is propagated in x-direction with the advection speed U_∞, the shape of the vortex being preserved. As a result, an analytical solution, with which the results of numerical simulations can be compared, is available.

In all the calculations presented here, the values for C and R were chosen as follows:

$$C = 2, \quad R = 0.1. \tag{66}$$

The Euler equations were solved on both Cartesian uniform and distorted meshes with different levels of resolution ($\Delta x/R = 0.375,\ 0.25,\ 0.187,\ 0.125$). Periodic boundary conditions were imposed in both directions. Fig. 18 shows isolines of the solution for, resp., the CE and $\mathrm{CS2}^{\mathrm{c}}_{\mathrm{nu}}$ scheme after the vortex has propagated over a distance of 1.5 m. The CS3 scheme was unstable for the present simulation and therefore results are not shown. Fig. 19 shows a more quantitative comparison with the vorticity along the vertical line passing through the center of the vortex ($\Delta x/R = 0.25$). The results obtained with the compact scheme are in very good agreement with the exact solution, while the CE scheme produces significant errors. In Fig. 20 the streamwise component of the velocity along the horizontal line passing through the center of the vortex is presented and compared to the exact solution.

In Fig. 21, a more systematic analysis of the absolute error and order of accuracy is provided. The logarithm of the average error is plotted as a function of the logarithm of the mesh size. From these results the actual order of accuracy can be calculated and corresponds to the inclination of the curves in Fig. 21.

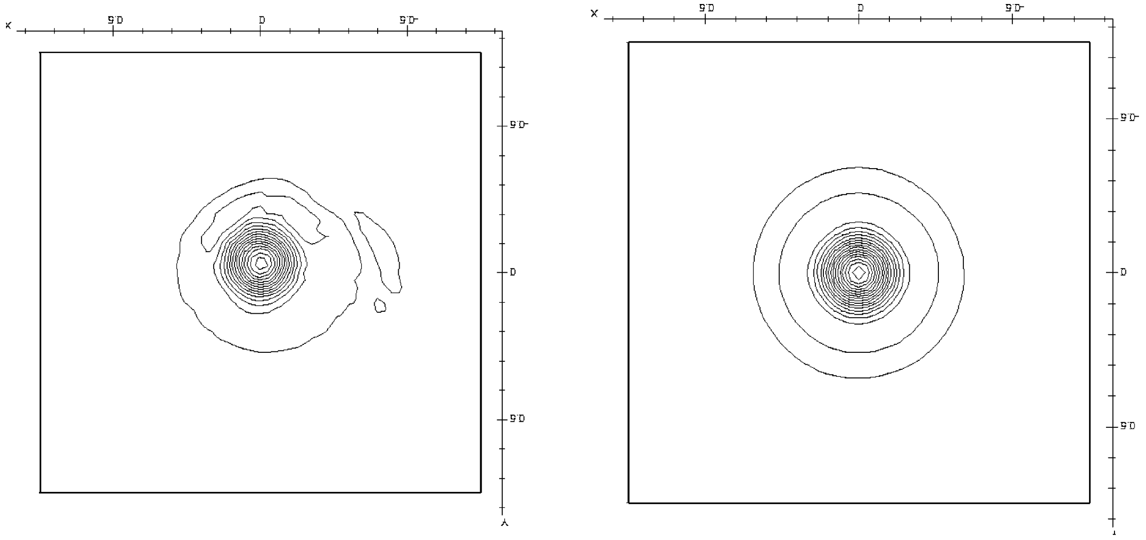

Fig. 18. Two-dimensional subsonic, vortical Euler flow on a Cartesian grid: isolines of the solution obtained with the CE scheme (left) and the CS^c_{nu} scheme (right).

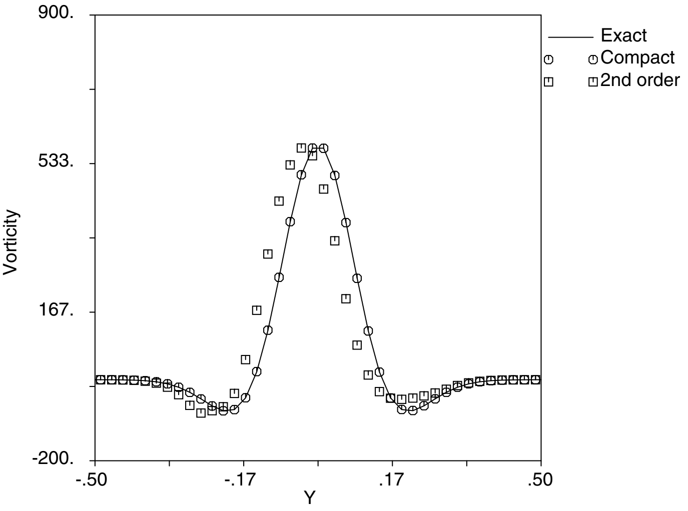

Fig. 19. Two-dimensional subsonic, vortical Euler flow on a Cartesian grid: vorticity along the vertical centerline with CE (squares) and CS^c_{nu} (circles) schemes.

The compact scheme $CS2^c_{nu}$ performs very well, with the measured order of accuracy (5.0) even higher than expected theoretically. This was also reported in [10], but the reason for this is not clear.

The benefit of using the proposed compact scheme can be estimated for this test case. From the plot in Fig. 21, one can evaluate how much finer the mesh needs to be for the CE scheme in order to produce a solution with an error level comparable to that of the CS^c_{nu} scheme. One finds that for a 40×40 mesh in case of the CS^c_{nu} scheme, one would need a 150×150 mesh for the CE scheme which has about 14 times more grid points. Taking into account that the present compact method, in its current implementation, is about

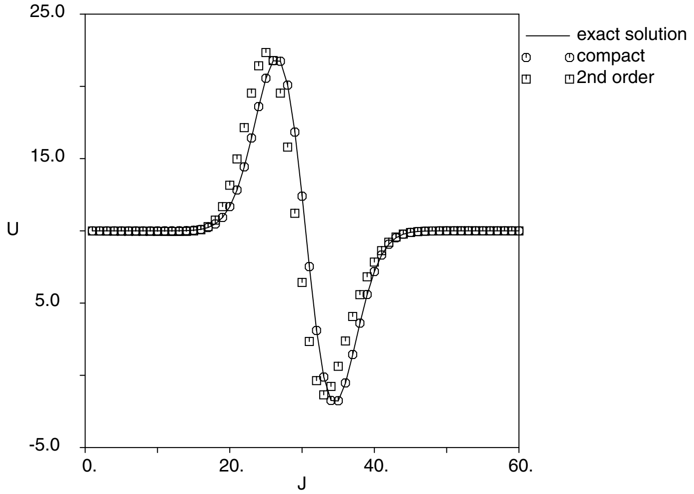

Fig. 20. Two-dimensional subsonic, vortical Euler flow on a Cartesian grid: streamwise component of velocity along the horizontal centerline with CE (squares) and CS_{nu}^{c} (circles) schemes.

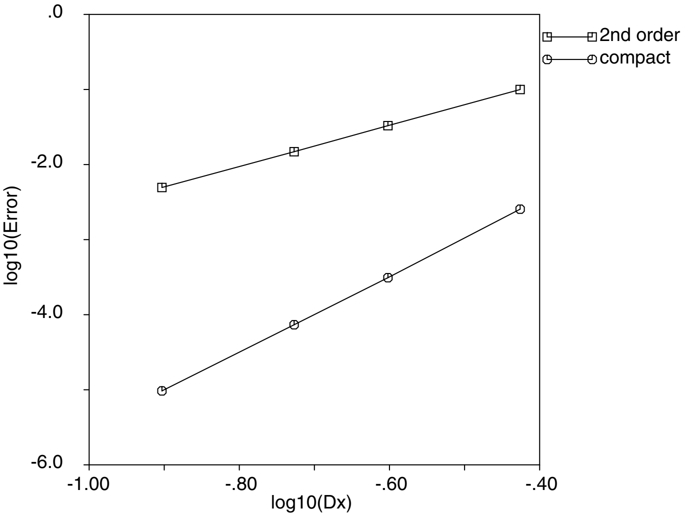

Fig. 21. Two-dimensional subsonic, vortical Euler flow on a Cartesian grid: grid refinement study of the mean error. CE (squares) and CS_{nu}^{c} (circles) schemes.

2.5 times more expensive in terms of CPU, one arrives at the conclusion that (at least for this test case) the proposed compact scheme is 5–6 times more efficient than the CE scheme.

A similar series of calculations was carried out on a sequence of curvilinear grids, one of which is shown in Fig. 22 .

Fig. 23 shows the isolines of the solution obtained with, resp., CE and CS_{nu}^{c} scheme. In Fig. 24 the streamwise component of the velocity along the vertical grid line through the center of the vortex is presented and compared to the exact solution. Again, the superior behaviour of the compact scheme in terms of accuracy is clearly confirmed. Also note there is a deterioration of the CE scheme results when switching from the Cartesian to the curvilinear grid. The solution shows some oscillatory behaviour in front of the

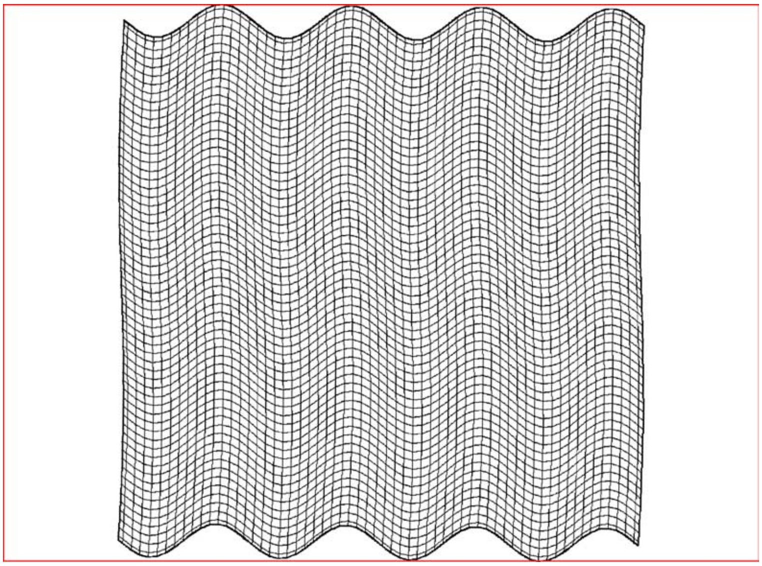

Fig. 22. The curvilinear grid used for the 2D subsonic, vortical Euler flow problem.

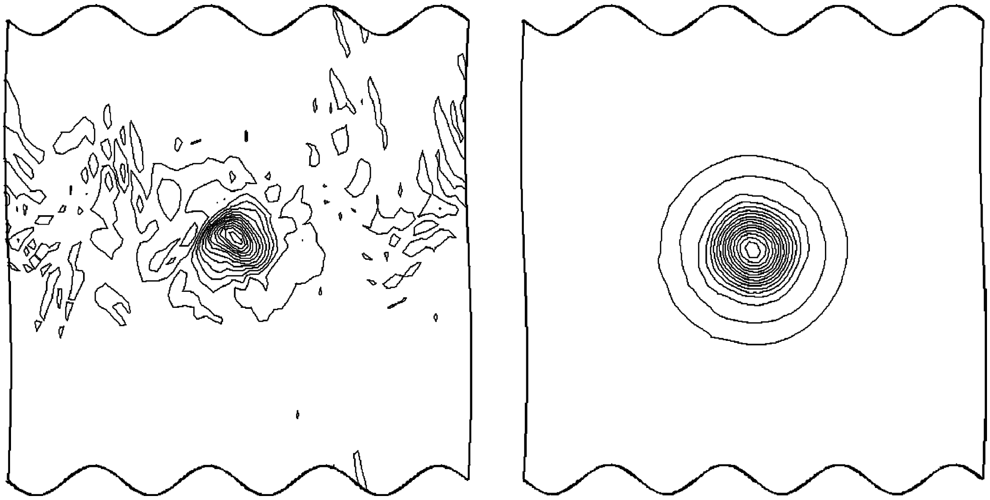

Fig. 23. Two-dimensional subsonic, vortical Euler flow on a curvilinear grid: isolines of the solution obtained with the CE scheme (left) and the $\mathrm{CS}^{\mathrm{c}}_{\mathrm{nu}}$ scheme (right).

velocity peak and the overshoot is also slightly higher on the curvilinear grid. Such deterioration is not found for the $\mathrm{CS}^{\mathrm{c}}_{\mathrm{nu}}$ scheme.

6.4. LES of channel flow

The capability of Padé type schemes to accurately represent the short length scales of the solution makes them very attractive for direct and large-eddy simulations of turbulence. To test the proposed formulation of

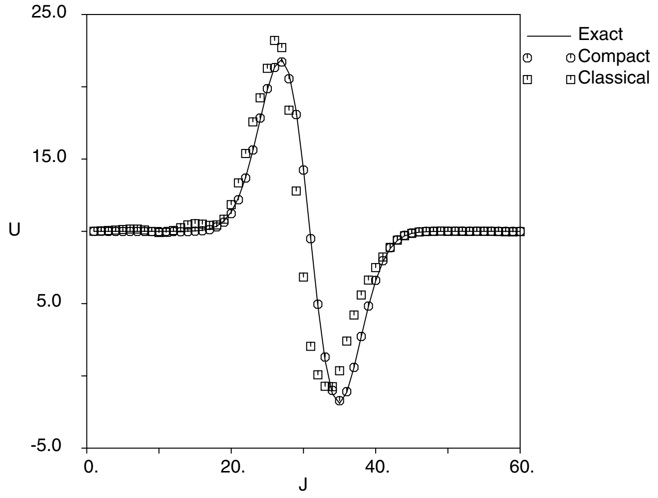

Fig. 24. Two-dimensional subsonic, vortical Euler flow on a curvilinear grid: the streamwise component of velocity along vertical grid line passing through the center of the vortex. CE (squares) and CS^c_{nu} (circles) schemes.

compact schemes in the context of these applications, the periodic channel flow was simulated by means of LES. The Reynolds number based on channel half width and wall friction velocity was 180. The dimensions of the computational domain were chosen 4π (streamwise direction), 2 (normal direction from wall to wall), and $4\pi/3$ (spanwise direction). Periodicity was assumed in both streamwise and spanwise directions. A source term acounting for the pressure difference in streamwise direction was added to the streamwise component of the momentum equation. The mesh used for the calculations was $33 \times 65 \times 33$, in respectively, streamwise, normal, and spanwise directions with hyperbolic tangent clustering from wall to wall. As subgrid-scale closure model, the Smagorinsky model [28] with a constant coefficient ($C_s = 0.07$) was used,

$$\nu_t = C_s (d\Delta)^2 \sqrt{2 S_{i,j} S_{i,j}}. \tag{67}$$

To force the subgrid-scale stresses to vanish at the walls the following damping function was used:

$$d = \left[1 - \exp\left(-\frac{y_+}{25} \right)^3 \right]^{1/2}. \tag{68}$$

The $CS2^c_{nu}$ scheme was used in homogeneous directions and the CE scheme was used in the direction from wall to wall. The obtained results are compared with those obtained using the CE scheme in all directions.

In Fig. 25 the calculated mean streamwise velocity profile is shown. Results obtained with the CE scheme in all directions are marked with square symbols whereas circles correspond to the solution obtained using the $CS2^c_{nu}$ scheme in homogeneous directions. Both results were obtained on the same mesh and with the same closure model. As a reference, results obtained with the CE scheme but with a dynamic Smagorinsky subgrid-scale model [29] and DNS results of Kim et al. [30] are shown. The improvement resulting from using the compact method is significant, the LES solution being close to the DNS solution. This improvement might be explained by the better resolution in the spanwise direction. It is known that this is especially important in LES of channel flow. A similar improvement is observed when comparing the turbulent velocity fluctuations (Fig. 26). Although the peak in streamwise velocity fluctuations is still overestimated compared to DNS (which is typical for LES of channel flow), it is closer to the DNS results. The location of the peak is much better predicted and corresponds to that of the DNS results. Towards the

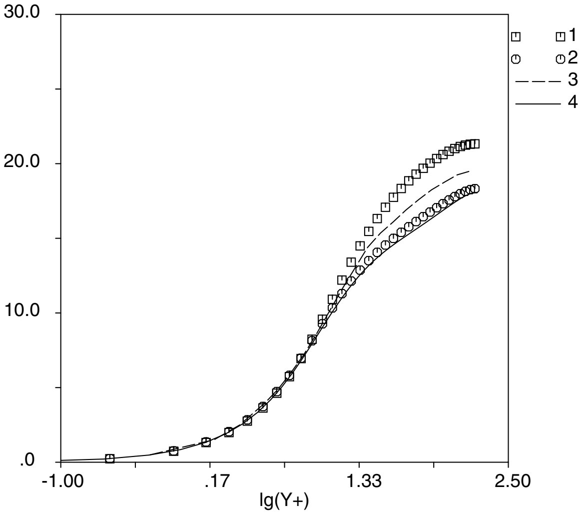

Fig. 25. LES of channel flow at $Re_\tau = 180$: mean streamwise velocity (1: CE scheme, $C_s = 0.07$; 2: CS^c_{nu} scheme, $C_s = 0.07$; 3: results Morinishi [29] (second-order scheme, dynamic subgrid-scale model); 4: DNS results Kim et al. [30]).

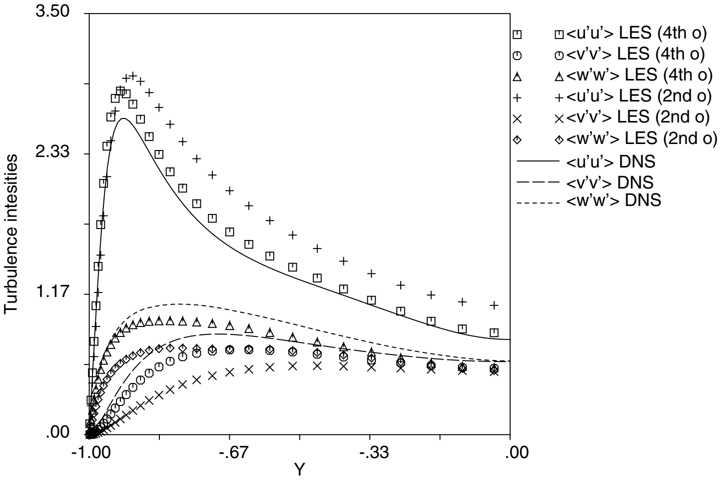

Fig. 26. LES of channel flow at $Re_\tau = 180$: turbulence intensities obtained with CE and CS^c_{nu} schemes.

center of the channel the agreement with DNS is clearly superior. Similar observations can be made for the transverse velocity fluctuations. Whereas the CE results start deviating from the DNS results immediately off the wall, the compact results follow the DNS results more closely, especially for the spanwise (w) fluctuations.

7. Conclusions

A new compact scheme has been formulated in the finite-volume context. The proposed approach is applicable to the solution of unsteady compressible Navier–Stokes equations on arbitrary meshes. The metrics of the grid are taken directly into account, without the use of a coordinate transformation. To test the method, a series of numerical experiments has been carried out for a 1D and 2D model problem, a subsonic vortical 2D Euler problem, and a 2D laminar flat plate. The schemes were then used in the LES simulation of the channel flow at $Re = 3300$. A significant improvement in the quality and accuracy of the results was obtained as compared to classical finite-volume methods.

Acknowledgements

This research work was partially funded by the Flemish Science Foundation (FWO) under the grant G.0130.02. This support is gratefully acknowledged.

Appendix A

All variables in (34) are developed in 2D Taylor series around point O (Fig. 2). As $\widetilde{u}_{i-1/2,j},\ \widetilde{u}_{i+1/2,j},\ \widetilde{u}_{i+3/2,j}$ are line integrals and $\overline{u}_{i+n,j+m}$ are area integrals , these Taylor series have to be integrated over the interfaces $(i-1/2,j),\ (i+1/2,j),\ (i+3/2,j)$ and the cells shown in Fig. 2. This results in an equation containing terms in

$$u_{\mathrm{O}},\quad \left.\frac{\partial u}{\partial x}\right|_{\mathrm{O}},\quad \left.\frac{\partial u}{\partial y}\right|_{\mathrm{O}},\quad \left.\frac{\partial^2 u}{\partial x^2}\right|_{\mathrm{O}},\quad \left.\frac{\partial^2 u}{\partial x\,\partial y}\right|_{\mathrm{O}},\quad \left.\frac{\partial^2 u}{\partial y^2}\right|_{\mathrm{O}},\quad \left.\frac{\partial^3 u}{\partial x^3}\right|_{\mathrm{O}},\quad \left.\frac{\partial^3 u}{\partial x^2\,\partial y}\right|_{\mathrm{O}},\quad \left.\frac{\partial^3 u}{\partial x\,\partial y^2}\right|_{\mathrm{O}},\quad \left.\frac{\partial^3 u}{\partial y^3}\right|_{\mathrm{O}},\ldots \tag{A.1}$$

Equating coefficients of the term in u_{O} in left-hand and right-hand side gives an equation for $\beta,\ \gamma,\ a_{n,m}$ (Eq. (A.2). By satisfying this relation. one ensures that (34)) is first-order accurate. Equating coefficients of the next two terms (in $\partial u/\partial y|_{\mathrm{O}},\ \partial^2 u/\partial x^2|_{\mathrm{O}}$) gives two additional equations, which, together with the first one, are conditions for second-order accuracy of (34).

The 10 relations that have to be satisfied in order to achieve a fourth-order accurate Padé type formula for approximation of the fluxes on the interfaces are:

$$\beta + 1 + \gamma = \sum_{n=0}^{1}\sum_{m=-1}^{1} a_{n,m}, \tag{A.2}$$

$$2\beta\Delta x_{i,j} + 2\gamma\Delta x_{i+1,j} = \sum_{n=0}^{1}\sum_{m=-1}^{1} a_{n,m}T^{x}_{i+n,j+m}, \tag{A.3}$$

$$2\beta\Delta y_{i,j} + 2\gamma\Delta y_{i+1,j} = \sum_{n=0}^{1}\sum_{m=-1}^{1} a_{n,m}T^{y}_{i+n,j+m}, \tag{A.4}$$

$$\beta\left(2\Delta x^2_{i,j} + \frac{1}{24}\Delta X^2_{i-1/2}\right) + \frac{1}{24}\Delta X^2_{i+1/2} + \gamma\left(2\Delta x^2_{i+1,j} + \frac{1}{24}\Delta X^2_{i+3/2}\right) = \sum_{n=0}^{1}\sum_{m=-1}^{1} a_{n,m}T^{x^2}_{i+n,j+m}\bigg/ 2, \tag{A.5}$$

$$\beta\left(4\Delta x_{i,j}\Delta y_{i,j}+\frac{1}{12}\Delta X_{i-1/2}\Delta Y_{i-1/2}\right)+\frac{1}{12}\Delta X_{i+1/2}\Delta Y_{i+1/2}+\gamma\left(4\Delta x_{i+1,j}\Delta y_{i+1,j}+\frac{1}{12}\Delta X_{i+3/2}\Delta Y_{i+3/2}\right)$$
$$=\sum_{n=0}^{1}\sum_{m=-1}^{1}a_{n,m}T^{xy}_{i+n,j+m}, \tag{A.6}$$

$$\beta\left(2\Delta y^2_{i,j}+\frac{1}{24}\Delta Y^2_{i-1/2}\right)+\frac{1}{24}\Delta Y^2_{i+1/2}+\gamma\left(2\Delta y^2_{i+1,j}+\frac{1}{24}\Delta Y^2_{i+3/2}\right)=\sum_{n=0}^{1}\sum_{m=-1}^{1}a_{n,m}T^{y^2}_{i+n,j+m}\Big/2, \tag{A.7}$$

$$\beta\left(\frac{4}{3}\Delta x^3_{i,j}+\frac{1}{12}\Delta x_{i,j}\Delta X^2_{i-1/2}\right)+\gamma\left(\frac{4}{3}\Delta x^3_{i+1,j}+\frac{1}{12}\Delta x_{i+1,j}\Delta X^2_{i+3/2}\right)=\sum_{n=0}^{1}\sum_{m=-1}^{1}a_{n,m}T^{x^3}_{i+n,j+m}\Big/6, \tag{A.8}$$

$$\beta\left[4\Delta x^2_{i,j}\Delta y_{i,j}+\frac{1}{12}\left(\Delta y_{i,j}\Delta X^2_{i-1/2}+2\Delta x_{i,j}\Delta X_{i-1/2}\Delta Y_{i-1/2}\right)\right]+\gamma\left[4\Delta x^2_{i+1,j}\Delta y_{i+1,j}\right.$$
$$\left.+\frac{1}{12}\left(\Delta y_{i+1,j}\Delta X^2_{i+3/2}+2\Delta x_{i+1,j}\Delta X_{i+3/2}\Delta Y_{i+3/2}\right)\right]=\sum_{n=0}^{1}\sum_{m=-1}^{1}a_{n,m}T^{x^2y}_{i+n,j+m}\Big/2, \tag{A.9}$$

$$\beta\left[4\Delta x_{i,j}\Delta y^2_{i,j}+\frac{1}{12}\left(\Delta x_{i,j}\Delta Y^2_{i-1/2}+2\Delta y_{i,j}\Delta X_{i-1/2}\Delta Y_{i-1/2}\right)\right]$$
$$+\gamma\left[4\Delta x_{i+1,j}\Delta y^2_{i+1,j}+\frac{1}{12}\left(\Delta x_{i+1,j}\Delta Y^2_{i+3/2}+2\Delta y_{i+1,j}\Delta X_{i+3/2}\Delta Y_{i+3/2}\right)\right]$$
$$=\sum_{n=0}^{1}\sum_{m=-1}^{1}a_{n,m}T^{xy^2}_{i+n,j+m}\Big/2, \tag{A.10}$$

$$\beta\left(\frac{4}{3}\Delta y^3_{i,j}+\frac{1}{12}\Delta y_{i,j}\Delta Y^2_{i-1/2}\right)+\gamma\left(\frac{4}{3}\Delta y^3_{i+1,j}+\frac{1}{12}\Delta y_{i+1,j}\Delta Y^2_{i+3/2}\right)=\sum_{n=0}^{1}\sum_{m=-1}^{1}a_{n,m}T^{y^3}_{i+n,j+m}\Big/6, \tag{A.11}$$

where

$$\Delta x_{i,j}=x_{i,j}-x_{\mathrm{O}},\quad \Delta y_{i,j}=y_{i,j}-y_{\mathrm{O}}. \tag{A.12}$$

($x_{i,j}$ and $y_{i,j}$ are the coordinates of the center of the cell i,j, Fig. 2)

$$\Delta X_{i-1/2}=x_{B'}-x_{A'},\quad \Delta X_{i+1/2}=x_B-x_A,\quad \Delta X_{i-1/2}=x_{B''}-x_{A''}, \tag{A.13}$$

$$\Delta Y_{i-1/2}=y_{B'}-y_{A'},\quad \Delta Y_{i+1/2}=y_B-y_A,\quad \Delta Y_{i-1/2}=y_{B''}-y_{A''}, \tag{A.14}$$

$$T^x_{i+n,j+m}=\frac{Q^x_{i+n,j+m}+\Delta x_{i+n,j+m}S_{i+n,j+m}}{S_{i+n,j+m}}, \tag{A.15}$$

$$T^y_{i+n,j+m}=\frac{Q^y_{i+n,j+m}+\Delta y_{i+n,j+m}S_{i+n,j+m}}{S_{i+n,j+m}}, \tag{A.16}$$

$$T^{x^2}_{i+n,j+m} = \frac{1}{S_{i+n,j+m}}\left(Q^{x^2}_{i+n,j+m} + 2\Delta x_{i+n,j+m}Q^{x}_{i+n,j+m} + \Delta x^2_{i+n,j+m}S_{i+n,j+m}\right), \tag{A.17}$$

$$T^{xy}_{i+n,j+m} = \frac{1}{S_{i+n,j+m}}\left(Q^{xy}_{i+n,j+m} + \Delta y_{i+n,j+m}Q^{x}_{i+n,j+m} + \Delta x_{i+n,j+m}Q^{y}_{i+n,j+m} + \Delta x_{i+n,j+m}\Delta y_{i+n,j+m}S_{i+n,j+m}\right), \tag{A.18}$$

$$T^{y^2}_{i+n,j+m} = \frac{1}{S_{i+n,j+m}}\left(Q^{y^2}_{i+n,j+m} + 2\Delta y_{i+n,j+m}Q^{y}_{i+n,j+m} + \Delta y^2_{i+n,j+m}S_{i+n,j+m}\right), \tag{A.19}$$

$$T^{x^3}_{i+n,j+m} = \frac{1}{S_{i+n,j+m}}\left(Q^{x^3}_{i+n,j+m} + 3\Delta x_{i+n,j+m}Q^{x^2}_{i+n,j+m} + 3\Delta x^2_{i+n,j+m}Q^{x}_{i+n,j+m} + \Delta x^3_{i+n,j+m}S_{i+n,j+m}\right), \tag{A.20}$$

$$\begin{aligned} T^{x^2y}_{i+n,j+m} = \frac{1}{S_{i+n,j+m}}\Big(&Q^{x^2y}_{i+n,j+m} + \Delta y_{i+n,j+m}Q^{x^2}_{i+n,j+m} + 2\Delta x_{i+n,j+m}Q^{xy}_{i+n,j+m} \\ &+ 2\Delta x_{i+n,j+m}\Delta y_{i+n,j+m}Q^{x}_{i+n,j+m} + \Delta x^2_{i+n,j+m}Q^{y}_{i+n,j+m} + \Delta x^2_{i+n,j+m}\Delta y_{i+n,j+m}S_{i+n,j+m}\Big), \end{aligned} \tag{A.21}$$

$$\begin{aligned} T^{xy^2}_{i+n,j+m} = \frac{1}{S_{i+n,j+m}}\Big(&Q^{xy^2}_{i+n,j+m} + \Delta x_{i+n,j+m}Q^{y^2}_{i+n,j+m} + 2\Delta y_{i+n,j+m}Q^{xy}_{i+n,j+m} \\ &+ 2\Delta x_{i+n,j+m}\Delta y_{i+n,j+m}Q^{y}_{i+n,j+m} + \Delta y^2_{i+n,j+m}Q^{x}_{i+n,j+m} + \Delta x_{i+n,j+m}\Delta y^2_{i+n,j+m}S_{i+n,j+m}\Big), \end{aligned} \tag{A.22}$$

$$T^{y^3}_{i+n,j+m} = \frac{1}{S_{i+n,j+m}}\left(Q^{y^3}_{i+n,j+m} + 3\Delta y_{i+n,j+m}Q^{y^2}_{i+n,j+m} + 3\Delta y^2_{i+n,j+m}Q^{y}_{i+n,j+m} + \Delta y^3_{i+n,j+m}S_{i+n,j+m}\right), \tag{A.23}$$

$$Q^{x^{\mathrm{s}}y^{\mathrm{p}}}_{i,j} = \int\int_{\Omega_{i,j}} (x - x_{i,j})^{\mathrm{s}}(y - y_{i,j})^{\mathrm{p}}\,\mathrm{d}x\,\mathrm{d}y, \tag{A.24}$$

and $\Omega_{i,j}$ is the area of the cell i, j

References

[1] S.K. Lele, Compact finite difference schemes with spectral-like resolution, J. Comput. Phys. 103 (1992) 16–42.

[2] J.W. Kim, D.J. Lee, Optimized compact finite difference schemes with maximum resolution, AIAA J. 34 (5) (1996).

[3] L. Gamet, F. Ducros, F. Nicoud, T. Poinsot, Compact finite difference schemes on non-uniform meshes. Application to direct numerical simulations of compressible flows, Int. J. Numer. Methods Fluids 29 (1999) 159–191.

[4] B.J. Boersma, S.K. Lele, Large eddy simulation of a mach 0.9 turbulent jet, AIAA paper 99-1874, 1999.

[5] M. Meinke, W. Schröder, E. Krause, Th. Rister, A comparison of second- and sixth-order methods for large-eddy simulation, Comput. Fluids 31 (2001) 695–718.

[6] E.K. Koutsavdis, G.A. Blaisdell, A.S. Lyrintzis, Compact schemes with spatial filtering in computational aeroacoustics, AIAA J. 38 (2000) 713.

[7] A. Povitsky, P.J. Morris, A higher-order compact method in space and time based on parallel implementation of the Thomas algorithm y flow, J. Comput. Phys. 161 (2000) 182–203.

[8] L. Collatz, The Numerical Treatment of Differential Equations, Springer, 1966.

[9] L. Collatz, Hermitian methods for initial-value problems in partial differential equations, in: Proceedings of the Royal Irish Academy Conference on Numerical Analysis, Topics in Numerical Analysis.

[10] R.M. Visbal, V.D. Gaitonde, Higher-order-accurate methods for complex unsteady subsonic flows, in: AIAA paper 98-0131, 36th Aerospace Science Meeting, Reno, NV, 1998.

[11] D. Gaitonde, M. Visbal, Pade-type higher-order boundary filters for the Navier–Stokes equations, AIAA J. 38 (2000) 2103.
[12] R.M. Visbal, V.D. Gaitonde, On the use of higher-order finite-difference schemes on curvilinear and deforming meshes, J. Comput. Phys. 181 (2002) 155–185.
[13] X. Deng, M. Mao, High-order dissipative weighted compact nonlinear schemes for Euler and Navier–Stokes equations, AIAA Paper 2001-2626, 2001.
[14] K.S. Ravichandran, Higher oder KFVS algorithms using compact upwind difference operators, J. Comput. Phys. 130 (1997) 161–173.
[15] W.J. Goedheer, J.H.H.M. Potters, A compact finite difference scheme on a non-equidistant mesh, J. Comput. Phys. 61 (1985) 269–279.
[16] D. Gaitonde, J.S. Shang, Optimized compact-difference-based finite-volume schemes for linear wave phenomena, J. Comput. Phys. 138 (1997) 617–643.
[17] M.H. Kobayashi, On a class of padé finite volume methods, J. Comput. Phys. 156 (1999) 137–180.
[18] C. Lacor, S. Smirnov, M. Baelmans, A finite volume formulation for compact schemes on arbitrary meshes with applications to LES, in: N. Satofuka (Ed.), CFD 2000, 1st International Conference on CFD, Kyoto, 11–14/7/2000, Springer, pp. 479–484.
[19] M.J. Pereira, M.H. Kobayashi, C.J. Pereira, High order compact schemes in finite volume context, in: B. Suarez, E. Onate, G. Bugeda, (Eds.), ECCOMAS 2000, Barcelona, CIMNE, 2000.
[20] J.M.C. Pereira, M.H. Kobayashi, J.C.F. Pereira, A fourth-order-accurate finite volume compact method for the incompressible Navier–Stokes solutions, J. Comput. Phys. 167 (2001) 217–243.
[21] S. Smirnov, C. Lacor, M. Baelmans, A finite volume formulation for compact schemes with applications to LES, in: AIAA paper 2001-2546, AIAA 15th CFD Conference, 2001.
[22] R. Vichnevetsky, Math. Comput. Simul. 21 (1979) 170.
[23] N.A. Adams, K. Shariff, A high-resolution hybrid compact-ENO scheme for shock-turbulence interaction problems, J. Comput. Phys. 127 (1996) 27–51.
[24] O.C. Zienkiewicz, R.L. Taylor, The Finite Element Method, vol. 1, fourth ed., McGraw-Hill, New York, 1988.
[25] A. Jameson, W. Schmidt, E. Turkel, Numerical solutions of the Euler equations by finite volume methods with Runge–Kutta time stepping schemes, AIAA Paper 81-1259, January 1981.
[26] C.K.W. Tam, Computational aeroacoustics: issues and methods, in: AIAA paper 95-0677, AIAA 33rd Aerospace Sciences Meeting and Exhibit, 1995.
[27] T. Broeckhoven, S. Smirnov, Jan Ramboer, C. Lacor, Finite volume formulation of compact upwind and central schemes with artificial selective damping, in: CD-ROM Proceedings of the Second MIT Conference on Computational Fluid and Solid Mechanics, Boston, 17-20/6/2003, also: accepted for publication in special issue of SIAM J. Sci. Comput.
[28] J. Smagorinsky, General circulation experiments with the primitive equations, Mon. Weather Rev. 91 (1963) 99–164.
[29] Y. Morinishi, Conservative properties of finite difference schemes for incompressible flow, Center for Turbulence Research, Annual Research Briefs, 1995.
[30] J. Kim, P. Moin, R. Moser, Turbulence statistics in fully developed channel flow at low reynolds number, J. Fluid Mech. 177 (1987).